BGSG

Volume 59

Research Paper

Correspondence to:
Olga Sykioti
sykioti@noa.gr

DOI number:
http://dx.doi.org/10.12681/bgsg.31892

Keywords:
granitoid intrusion, Lavrion, Fe-Mn mineralization, remote sensing, reflectance spectroscopy, spectral index

Citation:
Sykioti, O., Ganas, A., Vasilatos, C., and Kypritidou, Z. (2023), Investigating the Capability of Sentinel-2 and Worldview-3 VNIR Satellite Data to Detect Mineralized Zones at an Igneous Intrusion in The Koutala Islet (Lavreotiki, Greece) Using Laboratory Mineralogical Analysis, Reflectance Spectroscopy and Spectral Indices. Bulletin Geological Society of Greece, 59, 175-213.

Publication History:
Received: 24/11/2022
Accepted: 04/01/2023
Accepted article online: 13/01/2023

The Editor wishes to thank two anonymous reviewers for their work with the scientific reviewing of the manuscript and Ms Emmanouela Konstantakopoulou for editorial assistance.

Investigating the capability of Sentinel-2 and Worldview-3 VNIR satellite data to detect mineralized zones at an igneous intrusion in the Koutala islet (Lavreotiki, Greece) using laboratory mineralogical analysis, reflectance spectroscopy and spectral indices

Olga Sykioti[1], Athanassios Ganas[2], Charalampos Vasilatos[3], Zacharenia Kypritidou[3]

[1]Institute of Astronomy, Astrophysics, Space Applications and Remote Sensing, National Observatory of Athens, Vas. Pavlou & I. Metaxa, GR-15236 Penteli, Greece, sykioti@noa.gr,
https://orcid.org/0000-003-1301-6450
[2]Institute of Geodynamics, National Observatory of Athens, Hill of the Nymphs, Thiseio, P.O. box 20048, GR-11810 Athens, Greece, aganas@noa.gr,
https://orcid.org/0000-0002-1937-3283
[3]Department of Geology and Geoenvironment, School of Science, National and Kapodistrian University of Athens, University Campus, GR-15784 Zografou, Greece, vasilatos@geol.uoa.gr zach-kyp@geol.uoa.gr,
https://orcid.org/0000-0001-6162-3402; https://orcid.org/0000-0003-0095-5563

Abstract

During the last decades, the rapid progress of remote sensing data processing for their utilization in detecting locations of possible sites linked to hydrothermal alteration and ores has gained increasing attention due to significant time and cost savings. In this study, we present the findings of a joint remote sensing and laboratory examination of a mineralization zone induced by a granitoid intrusion onshore the islet of "Koutala", in Lavreotiki, central Greece. Our objective is to investigate the potential of Sentinel-2 and WorldView-3 VNIR satellite data to detect and map oxidized ore zones and alteration minerals that are detected from laboratory analysis of samples and could be linked to Fe-Mn mineralization. Two approaches are followed, namely reflectance spectroscopy and spectral indices. In reflectance spectroscopy, the spectral signatures of all minerals detected in the study area are retrieved from spectral libraries. The signatures are resampled to Sentinel-2 and to WorldView-3 VNIR spectral bands. Continuum-removal is then applied and the diagnostic absorption features of each mineral are detected for each spectral band configuration. The dataset with the best

spectral configuration for mineral detection is then used for the production of mineral maps using the corresponding satellite image. The second approach involves the calculation of spectral indices, namely ferric, ferrous iron and hydroxyl-bearing alteration, on reflectance spectra. The ferric iron index is applied to both satellite datasets while the two other indices require the use of SWIR bands and therefore, they can be only calculated on Sentinel-2 data. All results show that laboratory and satellite data analyses results are consistent and complementary. WorldView-3 VNIR data seem to be sensitive only to the ferric and manganese phase. Sentinel-2 data seem to be capable to detect and map all alteration minerals that are potentially linked to Fe-Mn ore, including both ferric and ferrous phases. The mineral absorption and spectral indices maps show that in the investigated area, there is significant mineralization related to the granitoid intrusion. Hydrothermal alteration is observed on the entire surface of the islet but it seems to be stronger at the eastern part of the islet where the granitoid/schist contact is located. It is the first time that (i) minerals linked to a potential Fe-Mn ore are detected on the islet and (b) the corresponding alteration mineral maps are produced from satellite data, revealing their spatial distribution and providing indirect estimations of the degree of their presence.

Keywords: *granitoid intrusion, Lavrion, Fe-Mn mineralization, remote sensing, reflectance spectroscopy, spectral index.*

Περίληψη

Τις τελευταίες δεκαετίες, η αυξανόμενη πρόοδος στην επεξεργασία των δορυφορικών δεδομένων για την αξιοποίησή τους στον εντοπισμό πιθανών θέσεων υδροθερμικών εξαλλοιώσεων και παρουσίας ορυκτών πόρων έχει αποτελέσει αντικείμενο εντατικής έρευνας. Στην παρούσα εργασία, παρουσιάζουμε τα αποτελέσματα μιας μελέτης που συνδυάζει εργαστηριακές αναλύσεις και επεξεργασία δορυφορικών δεδομένων για την ορυκτολογική εξέταση ζώνης εξαλλοίωσης από την διείσδυση γρανιτοειδούς που εντοπίστηκε στην επιφάνεια της νησίδας «Κουτάλα» στην περιοχή της Λαυρεωτικής. Στόχος είναι η διερεύνηση της δυνατότητας των δορυφορικών δεδομένων Sentinel-2 και WorldView-3 VNIR στην ανίχνευση και χαρτογράφηση ορυκτών εξαλλοίωσης που ευρέθησαν κατά τις εργαστηριακές αναλύσεις δειγμάτων τα οποία πιθανώς να συνδέονται με μετάλλευμα Fe-Mn. Για τον σκοπό αυτό, εφαρμόστηκαν δύο μέθοδοι, φασματοσκοπία ανάκλασης και φασματικοί δείκτες. Στην πρώτη μέθοδο, συλλέγονται οι φασματικές υπογραφές όλων των ορυκτών που εντοπίστηκαν στην περιοχή από φασματικές βιβλιοθήκες. Κατόπιν εφαρμόζεται μετασχηματισμός των τιμών ανακλαστικότητας με την αφαίρεση του συνεχούς. Στη συνέχεια, αναζητώνται οι απορροφήσεις που χαρακτηρίζουν

αποκλειστικά το κάθε ορυκτό για τον κάθε αισθητήρα. Ο αισθητήρας του οποίου τα φασματικά κανάλια μπορούν και ανιχνεύουν τα περισσότερα ορυκτά εξαλλοίωσης επιλέγεται για την χαρτογράφησή τους. Η δεύτερη μέθοδος αφορά στον υπολογισμό και παραγωγή χαρτών φασματικών δεικτών, όταν διατίθενται τα απαραίτητα κανάλια. Ο δείκτης που ανιχνεύει τρισθενή σίδηρο υπολογίζεται και στους δύο δορυφορικούς αισθητήρες. Ο δισθενής σίδηρος και ο δείκτης εξαλλοίωσης υπολογίζονται μόνο με τα δεδομένα Sentinel-2 λόγω των δύο καναλιών που διαθέτει στο SWIR. Τα αποτελέσματα της μελέτης δείχνουν ότι οι εργαστηριακές μετρήσεις και η επεξεργασία των δορυφορικών δεδομένων συμφωνούν και είναι συμπληρωματικές. Τα δορυφορικά δεδομένα παρέχουν πληροφορία ως προς την χωρική κατανομή των ορυκτών πάνω στο νησί. Συγκεκριμένα, προκύπτει ότι τα δεδομένα WorldView-3 VNIR, ανιχνεύουν την παρουσία γκαιτίτη και Mn_οξειδίων/υδροξειδίων. Επιπλέον, τα δεδομένα Sentinel-2 φαίνεται ότι είναι ικανά να ανιχνεύσουν (ι) την εξαλλοίωση καθώς και (ιι) όλα τα ορυκτά που συνδέονται με πιθανή παρουσία Fe-Mn μεταλλεύματος, είτε έχουν τρισθενή είτε δισθενή σίδηρο στη σύστασή τους. Οι δορυφορικοί χάρτες δείχνουν ότι υπάρχει, σε διαφορετικό βαθμό, σημαντική εξαλλοίωση σε όλη την επιφάνεια του νησιού η οποία συνδέεται με την μαγματική διείσδυση. Ωστόσο, η εξαλλοίωση είναι πιο ισχυρή στο ανατολικό τμήμα της νησίδας όπου παρατηρείται και η επαφή σχιστολίθων/γρανιτοειδούς. Με την παρούσα μελέτη, για πρώτη φορά στη νησίδα (ι) γίνεται ανίχνευση και χαρτογράφηση ορυκτών που συνδέονται με πιθανή παρουσία Fe-Mn μεταλλεύματος και (ιι) παράγονται χάρτες ορυκτών εξαλλοίωσης οι οποίοι παρέχουν πληροφορία τόσο για την χωρική κατανομή των ορυκτών στην επιφάνεια όσο και έμμεσες εκτιμήσεις του βαθμού παρουσίας τους.

Λέξεις-κλειδιά: *γρανιτοειδές, Λαυρεωτική, μεταλλοφορία Fe-Mn, Τηλεπισκόπηση, φασματοσκοπία ανάκλασης, φασματικός δείκτης.*

1. INTRODUCTION

During the last three decades, the use of satellite imagery in geological mapping and mineral exploration has grown rapidly in order to detect mineralization-related alterations and associated ore deposits (Van der Meer et al., 2012; Van der Meer and Van der Werff, 2014; Van der Werff and Van der Meer, 2015, 2016; Ge et al., 2018(a), 2018(b); Hu et al., 2018; Van der Meer et al., 2018; Pour et al., 2019; Vasuki et al., 2019; Ferrier et al. 2019; Tompolidi et al., 2020; Anifadi et al., 2022). Recent multispectral satellites such as the Landsat Operational Land Imager (OLI), and the Advanced Spaceborne Thermal Emission and Reflection Radiometer (ASTER) have been the most widely used multispectral satellite sensors for the detection and mapping of minerals related to alteration, such as iron oxides, hydroxyl-bearing minerals, and

carbonates (Rowan and Mars, 2003; Rowan et al., 2006; Ferrier et al., 2010, 2016; Mars and Rowan, 2010; Hosseinjani et al., 2011; Pour et al., 2011; Rajendran et al., 2017; Yang et al., 2018; El Kati et al. 2018; Abubakar et al., 2019; Pour et al. 2019; Ferrier et al. 2019; Tompolidi et al. 2020; Vural et al., 2021), especially, when the satellites provide spectral information in the shortwave infrared (SWIR) part of the electromagnetic spectrum.

Since 2015, additional studies have been conducted in order to reveal the potential of Sentinel-2 (S-2) Multispectral Imager (MSI) in geological remote sensing, mineral exploration and discrimination (Mielke et al., 2014; Van der Meer and Van der Werff, 2014; Yokova et al., 2016; Hu et al., 2018; Adiri et al., 2020; Ge et al., 2020; Purwadi et al., 2020; Tompolidi et al., 2020; Lanfranchi et al., 2021; Soydan et al., 2021; Anifadi et al., 2022). Sentinel-2 provides spectral information in twelve spectral bands, namely ten (10) in the visible-near infrared (VNIR) and two (2) in the SWIR (Table 1). Furthermore, WorldView 3 (WV-3) is a commercial multispectral satellite, launched in August 2014, owned and operated by DigitalGlobe, Inc. It measures reflected radiation in eight (8) visible-near infrared (VNIR) spectral bands between 390 and 1050 nm and/or in eight (8) SWIR bands ranging from 1080 to 2380 nm in a very high spatial resolution (DigitalGlobe Inc., 2017). There are relatively few studies in mineral exploration that have been conducted using this type of data. These studies exploit all the satellite's available bands, both in VNIR and SWIR (Sun et al., 2017; Salehi et al., 2020; Park and Choi, 2021). In this study, only a WV-3 VNIR dataset, covering the study area, was available. In Table 1, we show the S-2 spectral bands and the corresponding WV-3 VNIR spectral bands.

In literature, various satellite image processing methods and techniques have been proposed for mineral discrimination and mineral exploration. In this study, we focus on two methods, namely (i) Reflectance Spectroscopy (or imaging spectroscopy) and (ii) Spectral Indices (SIs). In reflectance spectroscopy, focus is given on the analysis of spectral signatures measured in the VNIR, SWIR and thermal infrared (TIR) regions of the electromagnetic spectrum (Farmer, 1974; Hunt, 1977; Clark and Roush, 1984; Burns, 1993; Clark, 1999; Ganas and Ferrier, 2002; Kruse, 2010; Pour et al., 2011). Generally, Fe-oxides can be detected in the VNIR region (400–1000 nm) and hydrated minerals and carbonates can be detected in the SWIR region (1–3 μm) and TIR region (7–14 μm) (Hunt, 1977; Goetz and Rowan, 1981; Burns, 1993; Clark, 1999; Sabins, 1999; Ganas and Ferrier, 2002; Rowan and Mars, 2003; Kruse, 2010; Ninomiya and Fu, 2019).

Table 1. S-2 and WV-3 VNIR spectral bands (*). The S-2 bands are referred in abbreviation as "S*b*" and the WV-3 VNIR bands as "W*b*". The column "Center" shows the center wavelength of each spectral band (nm). The column "Width" indicates the width of each spectral band (in nm). The column "Res" shows the spatial resolution of each spectral band (in m).

Sentinel-2				**Worldview-3 VNIR**			
Band (S*b*)	Centre (nm)	Width (nm)	Res. (m)	Band *(Wb)*	Centre (nm)	Width (nm)	Res. (m)
1	443	20	10	1	425	50	1.33
2	490	65	10	2	480	60	1.33
3	560	35	10	3	545	70	1.33
				4	605	40	1.33
4	665	30	10	5	660	60	1.33
5	705	15	10				
6	740	15	10	6	725	40	1.33
7	783	20	10				
8	842	115	10	7	832	125	1.33
8A	865	20	10				
9	940	20	10	8	950	180	1.33
11	1610	90	10				
12	2190	180	10				

(*) The WV-3 VNIR dataset also includes a panchromatic image centered at 660 nm with 0.33 m spatial resolution.

In particular, the VNIR spectral bands provide spectral absorption features due to electronic transitions and therefore are used to map transition metal-bearing minerals such as iron-bearing minerals (Hunt, 1977; Hunt and Ashley, 1979; Clark and Roush, 1984; Burns, 1993; Cloutis, 1996; Clark, 1999; Sabins, 1999; Rowan and Mars, 2003; Rowan et al., 2003; Bishop and Murad, 2005; Kruse, 2012; Van der Meer et al., 2012). Apart from the original (e.g. reflectance) spectra, reflectance spectroscopy can also be applied to transformed spectra, such as continuum removed spectra. Continuum removal (CR) is defined via a function that isolates characteristic absorption areas in a given spectrum (Clark and Roush, 1984; Clark, 1999) and is applied on the original spectra. The continuum corresponds to the background signal related to all the other components of the image. This signal is removed, while maintaining only the targeted absorption feature (Kruse, 1988; Kruse et al., 1993; Clark, 1999). Spectrally, the targeted absorption feature depends on the chemistry of the mineral content, while its intensity is related to the amount of the abundance of the mineral in the pixel (Clark, 1999; Hunt and Ashley, 1979). This is quantified by the depth of diagnostic absorption feature(s) in the associated spectrum (Clark, 1999; Kruse, 1988; Kruse et al., 1993). In addition, among the oldest and most frequently used methods are Spectral Indices (SIs)

and band ratios. SIs are computed per pixel in an image. They involve measurements at certain spectral bands of the spectral signature of the pixel under study and they are mathematically expressed as a combination of these measurements via generally simple mathematical operations (Jackson, 1983). The aim of SIs is to enhance and quantify spectral differences due to different compositions within the image. In particular, SIs enhance the difference between a well-defined reflectance and a diagnostic absorption feature in the spectral signature of the pixel under study.

A special case of SIs is represented by band ratios, where the ratio of two spectral bands is computed. Several SIs have been proposed using a range of wavelength combinations for mapping various mineral assemblages (Cloutis, 1996; Sabins, 1999; Cudahy and Hewson, 2002; Yamaguchi and Naito, 2003; Henrich et al., 2009; Shim et al., 2021), especially after the arrival of ASTER data with their SWIR spectral bands (Abrams et al., 1983; Abrams & Hook, 1995; Yamaguchi et al., 1998; Yamagushi & Naito, 2003; Kalinowski and Oliver, 2004; Gad and Kusky, 2007; Rajendran et al., 2011; Abrams et al., 2015; Ferrier et al. 2016; Askari et al., 2018; Shuai et al., 2022). Depending on band availability, these SIs have also been adapted to Landsat 8 OLI and to Sentinel-2 spectral bands (Van der Meer et al., 2012; Van der Meer and Van der Werff, 2014; Van der Werff and Van der Meer, 2015, 2016).

Concerning lithological/mineral mapping applications in the Greek territory, there are several studies using various methods and techniques applied on multispectral and/or hyperspectral data. Indicative examples are the application of SIs on S-2, ASTER and/or Landsat 8 data (Anifadi et al., 2016; Ferrier et al. 2016; Tompolidi et al., 2020; Anifadi et al., 2022; Sykioti et al. 2022), spectral unmixing on (i) S-2, ASTER and Landsat 8 OLI data (Tompolidi et al., 2020) and (ii) EO-1 Hyperion hyperspectral data (Nikolakopoulos et al., 2007), Spectral Angle Mapping and Mixture-Tuned Matched Filtering on EO-1 Hyperion data (Nikolakopoulos et al., 2007), fusion techniques on EO-1 Hyperion and ALI for spatial resolution enhancement (Nikolakopoulos et al., 2010), PCA, ICA and Tasseled Cap techniques on EO-1 ALI data (Nikolakopoulos et al., 2018) and finally, supervised classification on Worldview-2 data (Oikonomidis et al., 2016).

In this paper, we present the findings of a joint remote-sensing and laboratory examination of a mineralization zone induced by the intrusion of a small igneous body onshore the islet of “Koutala”, in Lavreotiki, Greece (Fig.1). Our objective is to investigate the potential of S-2 and WV-3 VNIR data to detect and map alteration minerals which are detected from laboratory analysis of samples and could be linked to

Fe-Mn ore. The selection of these multispectral sensors in order to conduct this study is based on spectral criteria. First, there are no satellite hyperspectral acquisitions that cover the study area (i.e., EO-1 Hyperion archive data). Secondly, compared to other current multispectral sensors, these two sensors are the most suitable for this type of study since they both include several spectral bands within the VNIR area, which enable the detection iron-bearing minerals, and consequently Fe-Mn mineralization (Clark, 1999). Since a relatively high spectral resolution is needed for mapping iron contents with reflectance data, especially S-2 includes several, relatively narrow, bands that cover the 0.9 μm iron absorption feature, while, as aforementioned, other space-borne sensors traditionally used for geologic remote sensing, like ASTER and Landsat 8 OLI have only one band in this feature (van der Werff, 2015).

The adopted methodology includes a two-way approach, namely Reflectance Spectroscopy and SIs. The novelty of this paper lies on the fact that (i) Fe-Mn mineralization has never been detected on the Koutala islet of Lavreotiki, (ii) the Fe-Mn mineralization in the area has never been studied before with the use of S-2 and WV-3 VNIR data, (iii) it is the first time that Fe-Mn ore-related mineral maps are produced for the study area, (iv) it is the first time that indirect estimations of the degree of presence of Fe-Mn ore-related alteration minerals in the study area are provided through characteristic absorption features and SIs and finally (v) it is the first time that mineral spatial distribution information on the study area is provided additionally to the existing geological map and relative literature.

2. STUDY AREA

The islet of “Koutala” is located about 5 km NNE of the city of Lavrion (Fig. 1). The islet has a form of a rocky promontory, forming a characteristic tombolo feature with the mainland (in coastal geomorphologic terms). Its size is about 240 m in E-W by 40-60 in the N-S direction.

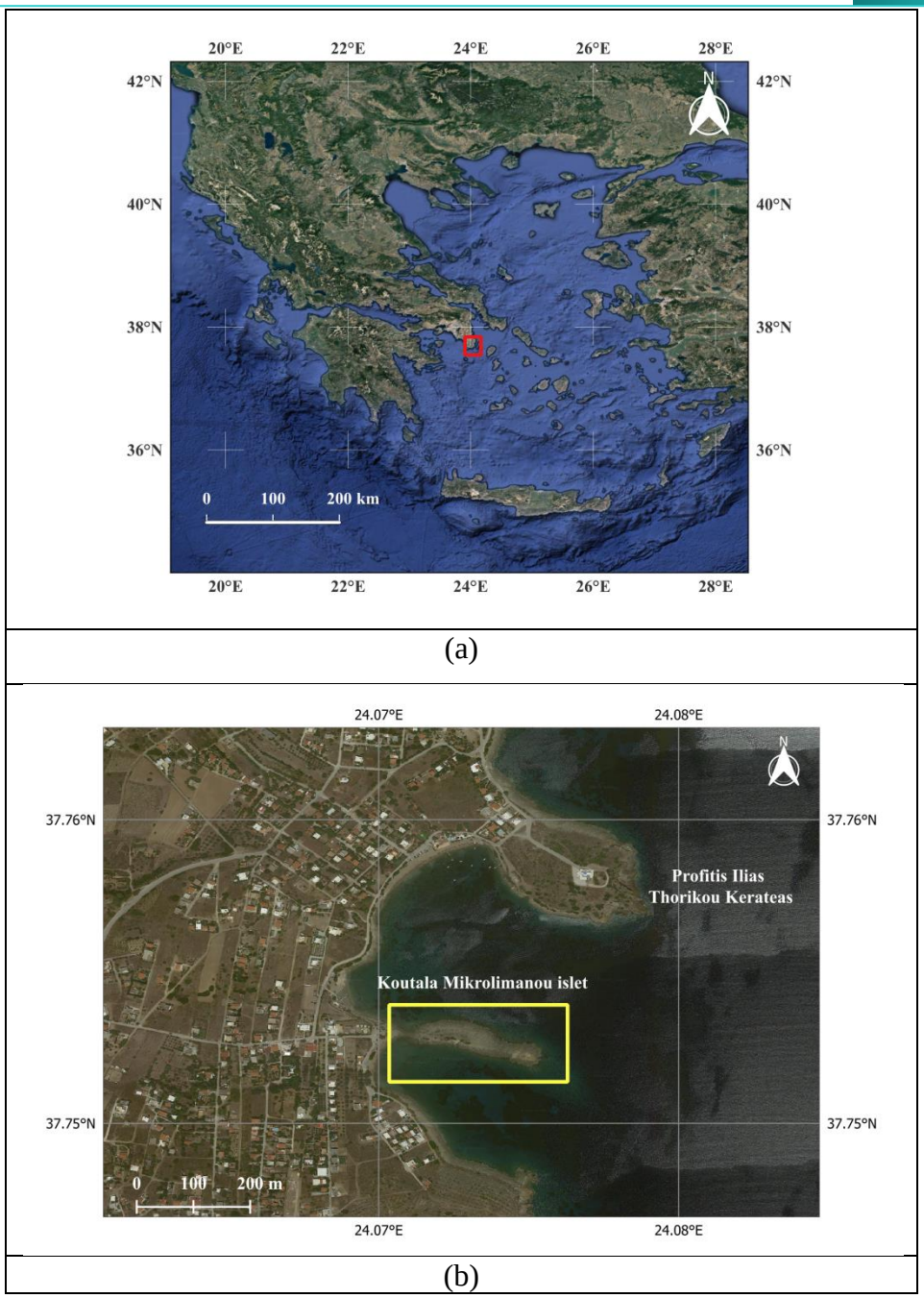

Fig. 1. Location of the study area: (a) Lavrion area in Attica (Greece) (red rectangle); (b) Koutala islet in Lavrion area (yellow rectangle). Background image from Google Earth.

2.1 Geological setting and mineralization

The general Lavreotiki area (Attica, Greece) belongs to the Attic-Cycladic Crystalline Belt (ACCB) representing a multistage metamorphic region which includes two major geological units; the lower tectonic unit (LTU) and the upper tectonic unit (Papanikolaou and Syskakis, 1991; Photiades and Carras, 2001; Upper Unit in Fig. 2) that represents the hanging-wall of the Cycladic extensional detachment. An extract of the geological map of the study area is shown in Fig. 2. In that area, the LTU consists of an "autochthonous" sequence of Triassic-Lower Jurassic metamorphic rocks, of

greenschist to amphibolite phases, that includes (i) the Lower marble series, (ii) the Kessariani schists and (iii) the Upper marble series, that are all overlain transgressively by Upper Jurassic-Lower Cretaceous non-metamorphic conglomerate and limestone formations (Fig. 2; Marinos and Petrascheck, 1956; Photiades and Carras, 2001). The LTU was overthrust by a phyllitic nappe of blueschist metamorphic phase (allochtonous sequence or Intermediate Tectonic Unit) of a probable Upper Cretaceous age (Marinos and Petrascheck, 1956; Papanikolaou and Syskakis, 1991; Photiades and Carras, 2001).

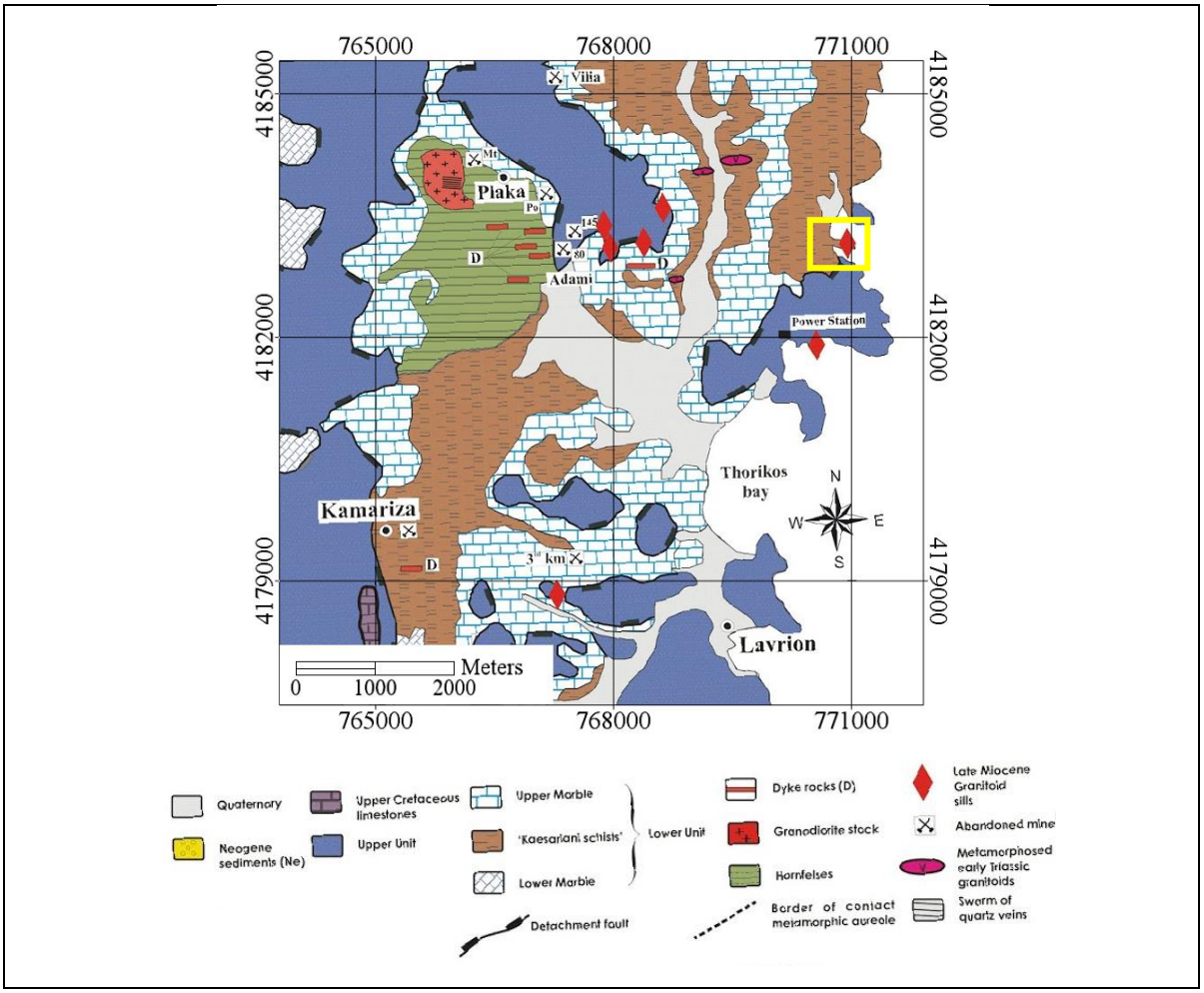

Fig. 2. Georeferenced (projection UTM34 - WGS84) digital extract of the geological map of the area after Skarpelis, (2007; modified after Marinos and Petraschek, 1956). The yellow rectangle shows the study area, where the red rhombus indicates the granitoid intrusion on the islet.

The well-known granodioritic intrusions in Lavreotiki peninsula are synchronous with the Miocene extensional detachment faulting as a part of a metamorphic core complex formation in the ACCB (Altherr et al., 1982; Pe-Piper and Piper, 2002; Skarpelis et al., 2007).

Mineralization in the ACCB is generally associated with the succeeding stages of the tectono-plutonic evolution and is strongly related to the extensional faulting (Skarpelis, 2002). Ascending hydrothermal fluids deposited massive sulphide ore in carbonate rocks (carbonate replacement deposit), while skarn-type mineralization has been formed, due to contact metamorphism, around the granitoid intrusions (Economou et al., 1981; Bonsall et al., 2007; Skarpelis and Argyraki, 2008; Voudouris et al., 2008; Berger et al., 2012; Voudouris et al., 2018). Late NW–SE trending tension gashes have acted as conduits for ascending hydrothermal fluid, resulting in the formation of mineralized veins (Skarpelis and Argyraki, 2008; Voudouris et al., 2008). Fe-Mn mineralization in Lavreotiki area is generally hosted within carbonate rocks, close to the surface of the detachment faults and the contacts between lower and upper marbles with the Kessariani schist. The characteristic features of that type of Fe-Mn mineralization seems to be the result of multistage supergene processes superimposed over initial hydrothermal stages (Vasilatos and Economou-Eliopoulos, 2018; Vasilatos et al., 2022). The occurrence of abundant bacteriomophic Fe-Mn-oxides/hydroxides in those deposits has been attributed by Vasilatos and Economou-Eliopoulos (2018) and Vasilatos et al. (2022) to bacteria-driven redox reactions during those ore-forming processes. However, typical iron-rich gossan formations are located at, or close to, the surface of the detachment fault. They had been formed during supergene processes by downward-penetrating water, oxidation of hypogene sulphide mineralization, mobilization of metals and re-precipitation, as a result of the interaction of acidic water with marble (Skarpelis and Argyraki, 2008).

3. MATERIALS AND METHODS

3.1 Materials

Field data

During a field campaign conducted on 18 July 2022, eighteen (18) GPS measurements were collected at the islet in order to delineate the contact between the granitoid and the schists (Fig. 3). The GPS data were collected using the RTK (real-time kinematic) technique that offers a positioning accuracy of the order of a few cm (e.g., Mekik and Arslanoglu, 2009). Furthermore, four (4) rock samples were collected and analyzed in the laboratory using the XRD method, one of schist (point 11 in Fig.3), two of granitoid (points 17 and 13 in Fig. 3) and one at the granitoid/schist contact (point 17 in Fig. 3).

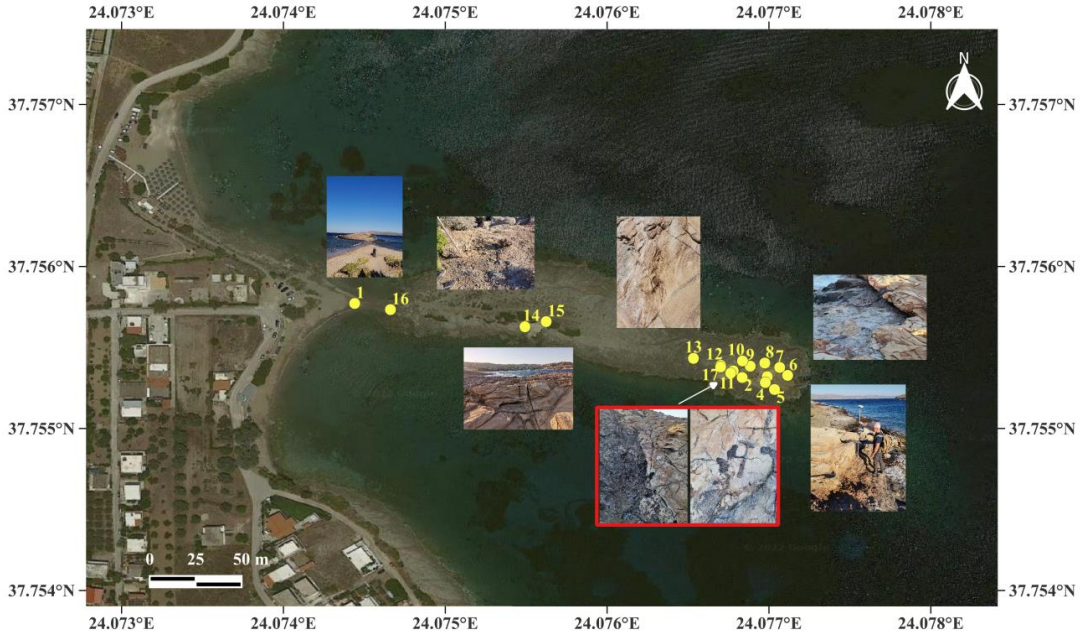

Fig. 3. Location of GPS measurements on the islet (yellow points) and photos of different locations in the field. In the red rectangle at the bottom of the image, two photos show the location of the schists/granitoid contact where the sample of granitoid/schist was collected. The background image is a Google Earth high resolution image, co-registered to the WV-3 VNIR image.

Spaceborne data

A Sentinel-2 Level 2A satellite image (S-2) was acquired on 19 July 2022 (Fig. 4a). The output reflectance image (pixel values ranging [0,1]) consists of 12 spectral bands, resampled to 10 m spatial resolution. Furthermore, a WV-3 VNIR multispectral dataset, including a panchromatic image, was retrieved, that was acquired on 15 January 2022 (Fig. 4b). The multispectral dataset consists of 8 spectral bands in the VNIR with 1.33 m spatial resolution (Table 1). An additional panchromatic image was provided centred at 660 nm with 0.33 m spatial resolution.

(a)

(b)

Fig. 4. True-colour composites of the two satellite subsets centred at the study area, (a) one from the Sentinel-2 image (acquired 19/7/2022, spatial resolution 10 m) and (b) one from the Worldview-3 VNIR image (acquired 15/1/2022, spatial resolution 1.33 m).

3.2 Methodology

The flowchart of the research methodology followed in this study is shown in Fig. 5.

3.2.1 XRD analysis

During the July 2022 field campaign, four rock samples were collected and analyzed in the laboratory of the Department of Geology at NKUA using the XRD method. X-ray powder diffraction (XRD) data were obtained using a Siemens Model 5005 X-ray diffractometer (Bruker AXS GmbH., Karlsruhe, Germany), Cu Ka radiation at 40 kV, 40 nA, 0.020 step size and 1.0 s. step time. The XRD patterns were evaluated using the EVA 10.0 program of the Siemens (Bruker AXS GmbH) DIFFRAC software package (NKUA). The evaluation of the acquired XRD patterns has identified, among other minerals, the presence of hydrothermal alteration minerals in all studied samples (Fig. 6).

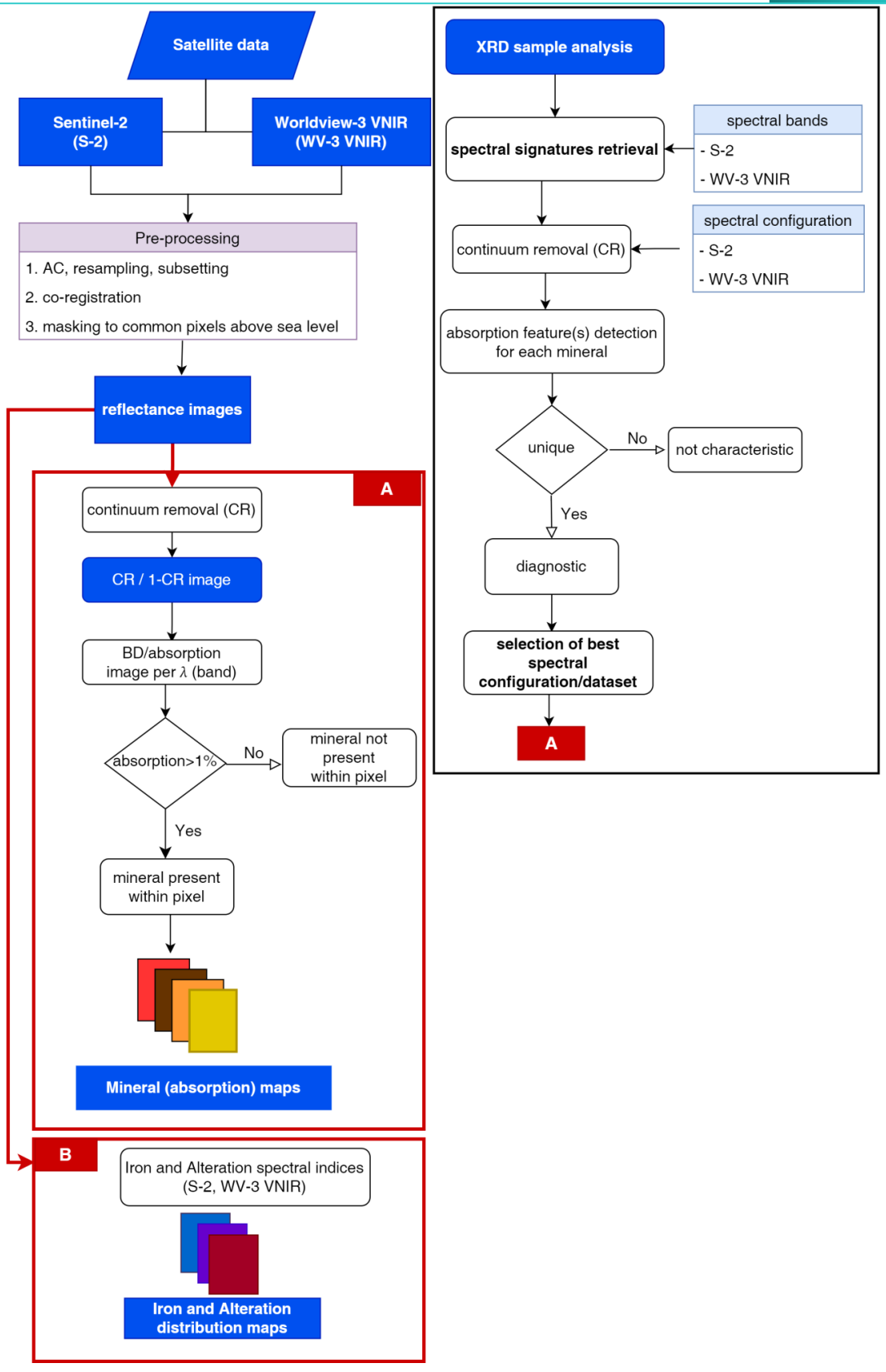

Fig. 5. Flowchart of the methodology followed in this study. Blue labels: datasets; A) reflectance spectroscopy procedure; B) SI procedure.

Micas and chlorite were determined in the granitoid and schist samples while goethite, Mn-oxide/hydroxides and micas were identified in the contact sample, indicative of Fe-

Mn mineralization. Mn-oxide/hydroxides were also identified in the schist sample (Fig. 6a). Table 2 summarizes the mineralogy of the lithologies present in the study area.

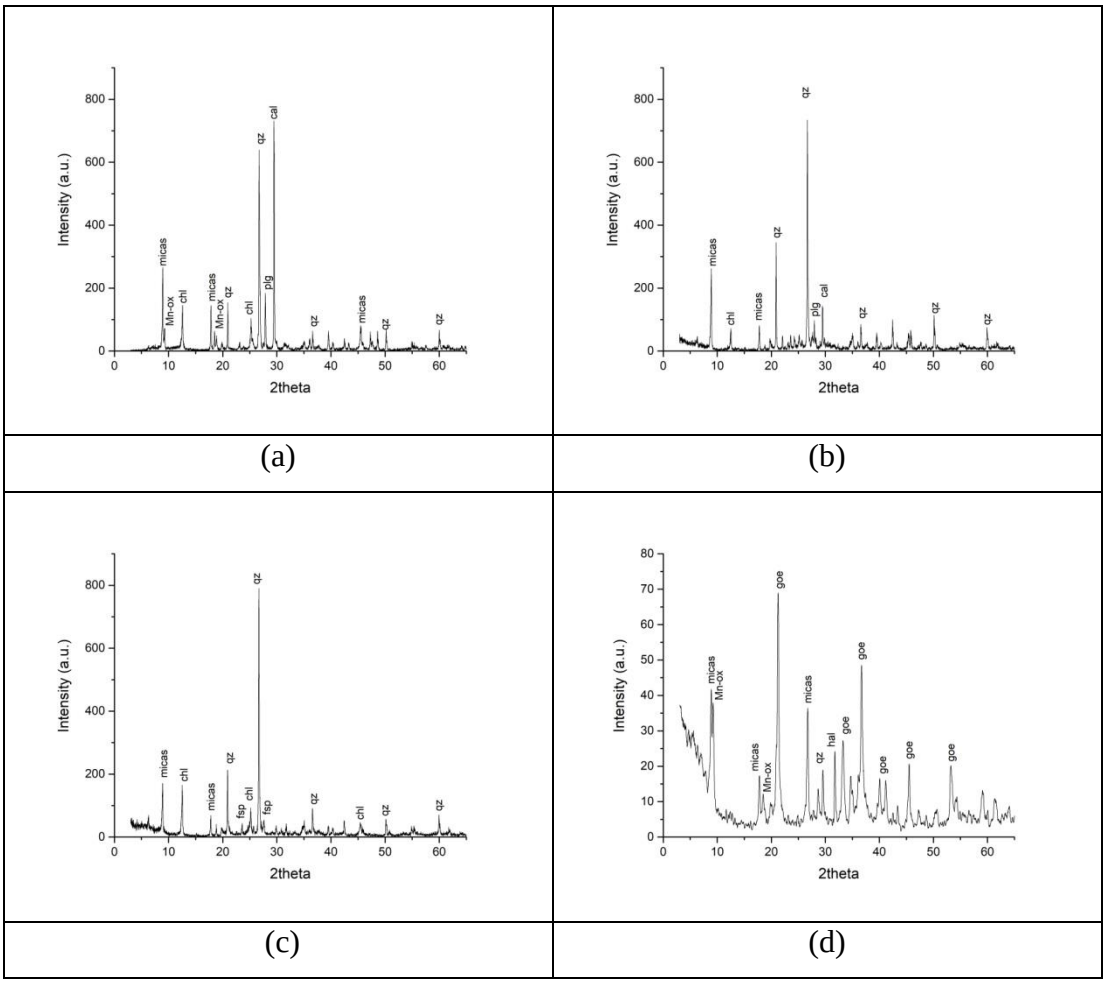

Fig. 6. XRD patterns of the samples collected in the field corresponding to (a) schists, (b) and (c) granodiorite and (d) granodiorite/schist contact.

Table 2. Mineralogy of the lithologies present in the study area according to XRD analysis results on the four samples collected in the field.

Phases	Abbr.	schist	Granodiorite-1	Granodiorite-2	contact
micas	micas	+	+	+	+
quartz	qz	+	+	+	+
chlorite	chl	+	+	+	
K-feldspars	fsp		+	+	
calcite	cal	+		+	+
plagioclase	plg	+		+	
Mn-oxides	Mn-ox	+			+
goethite	goe				+
halite	hal				+

3.2.2 Mineral spectral signatures – absorption feature analysis

Following the XRD results of the mineralogical analysis, the spectral signatures of the eight detected minerals (Table 2) are retrieved from the USGS Spectral Library Version 7 (https://crustal.usgs.gov/speclab/QueryAll07a.php) and one, for Mn_oxide/hydroxide, from the PDS Geosciences Node Spectral Library (https://pds-speclib.rsl.wustl.edu/). The spectral signatures retrieved from the USGS spectral library correspond to pure samples of average grain size 30-70 μm. They are retrieved from the database in two forms: one resampled to S-2 spectral bands and one to W-3 VNIR spectral bands. The original Mn_oxide/hydroxide spectral signature is also convolved to the S-2 and WV-3 VNIR spectral bands using the ENVI 5.5 software. The reflectance reference signatures (or spectral signatures as they are named hereafter) of all minerals are presented in Fig. 7a-i. Micas, chlorite, plagioclase and K-feldspar are represented by the retrieved spectral signatures of muscovite, clinochlore, andesine and orthoclase respectively (Fig. 7 c, d, e, f). Concerning the Mn_oxides/hydroxides, they are represented by the spectral signature of manganite (Fig. 7b).

A well-established processing technique in reflectance spectroscopy, namely continuum removal (CR), is then applied to the spectral signatures of pixels of the satellite images. According to this method, one determines for the spectral signature and/or each pixel' s spectrum, *x*, its *continuum*, which is a convex hull fit composed of straight-line segments that connect consecutive local maxima (Clark & Roush, 1984; Clark, 1999). The values of the first and last bands (e.g. *Sb*1 and *Sb*12 for S-2 spectral bands) in the continuum-removed (CR) spectrum are set to 1.0. The continuum is removed by dividing the convex hull into the actual spectrum *x*, as indicated by the general equation of continuum removal (Eq. 1); thus:

$$\boldsymbol{S_{cr}} = \frac{\boldsymbol{S}}{\boldsymbol{C}} \qquad \text{(Eq. 1)}$$

where $\boldsymbol{S_{cr}}$ is the continuum-removed spectrum, $\boldsymbol{S}$ is the original spectrum and $\boldsymbol{C}$ is the continuum.

Band values (called Band Depths, BDs) in the resulting CR spectrum are equal to 1.0 where no absorption feature is encountered and less than 1.0 where an absorption feature is present. In this study, this procedure is applied in two stages of the methodology, first on the mineral reference spectral signatures, resampled to S-2 12 spectral bands and WV-3 VNIR 8 spectral bands, and later, on the pixel spectra of the selected satellite image for the production of mineral maps.

On the CR reference spectral signatures of minerals, we examine whether each signature presents an absorption feature that does not exist in the other signatures (Fig. 7). If so, then this feature is characterized as diagnostic of the specific mineral. On the other hand, if this feature is also present in the spectral signature(s) of other mineral(s), then it is not taken into consideration. The satellite dataset that corresponds to the spectral configuration (S-2 and/or WV-3 VNIR spectral bands) that distinguishes the highest number (or all) of Fe-Mn ore-related minerals is then used for mineral mapping.

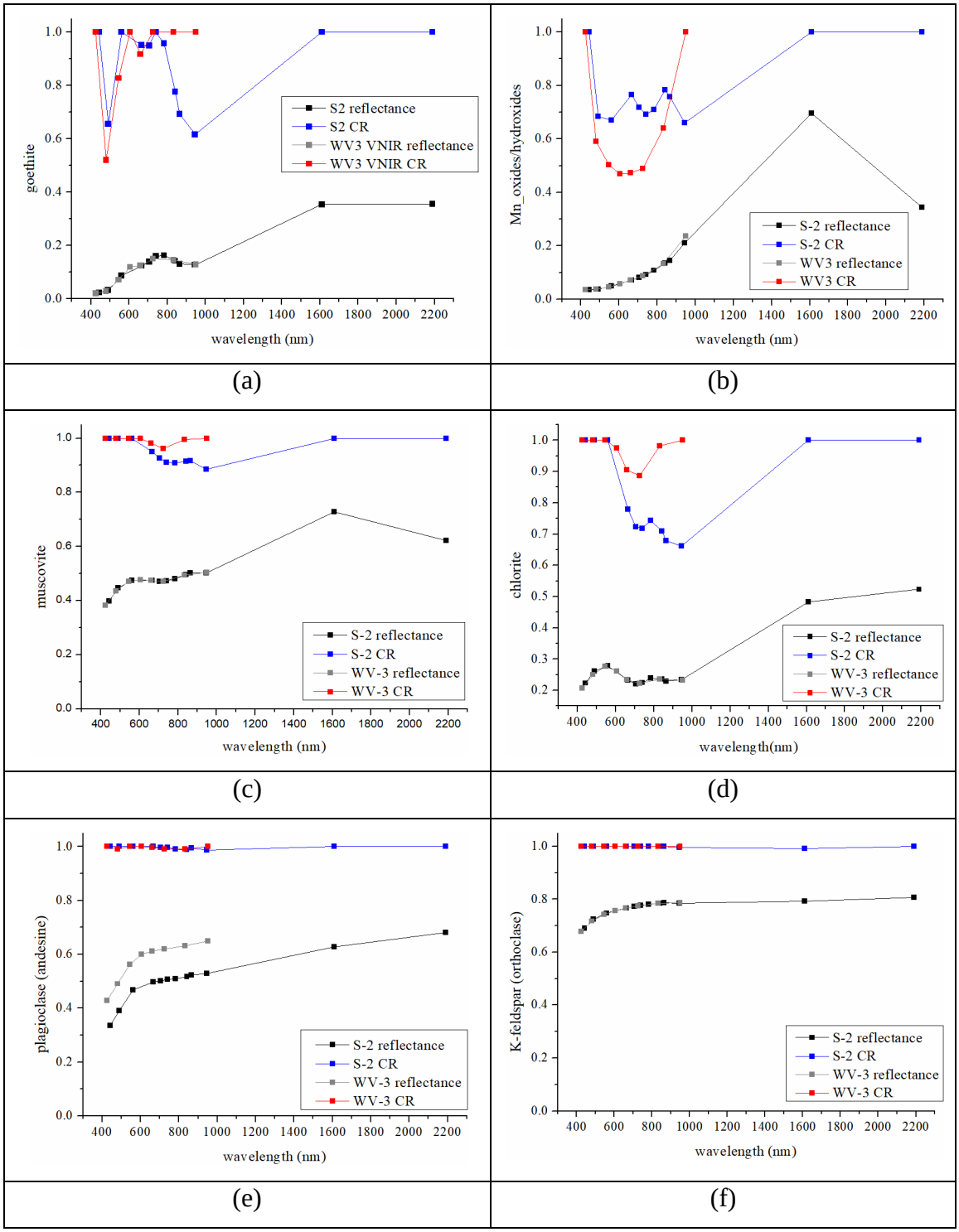

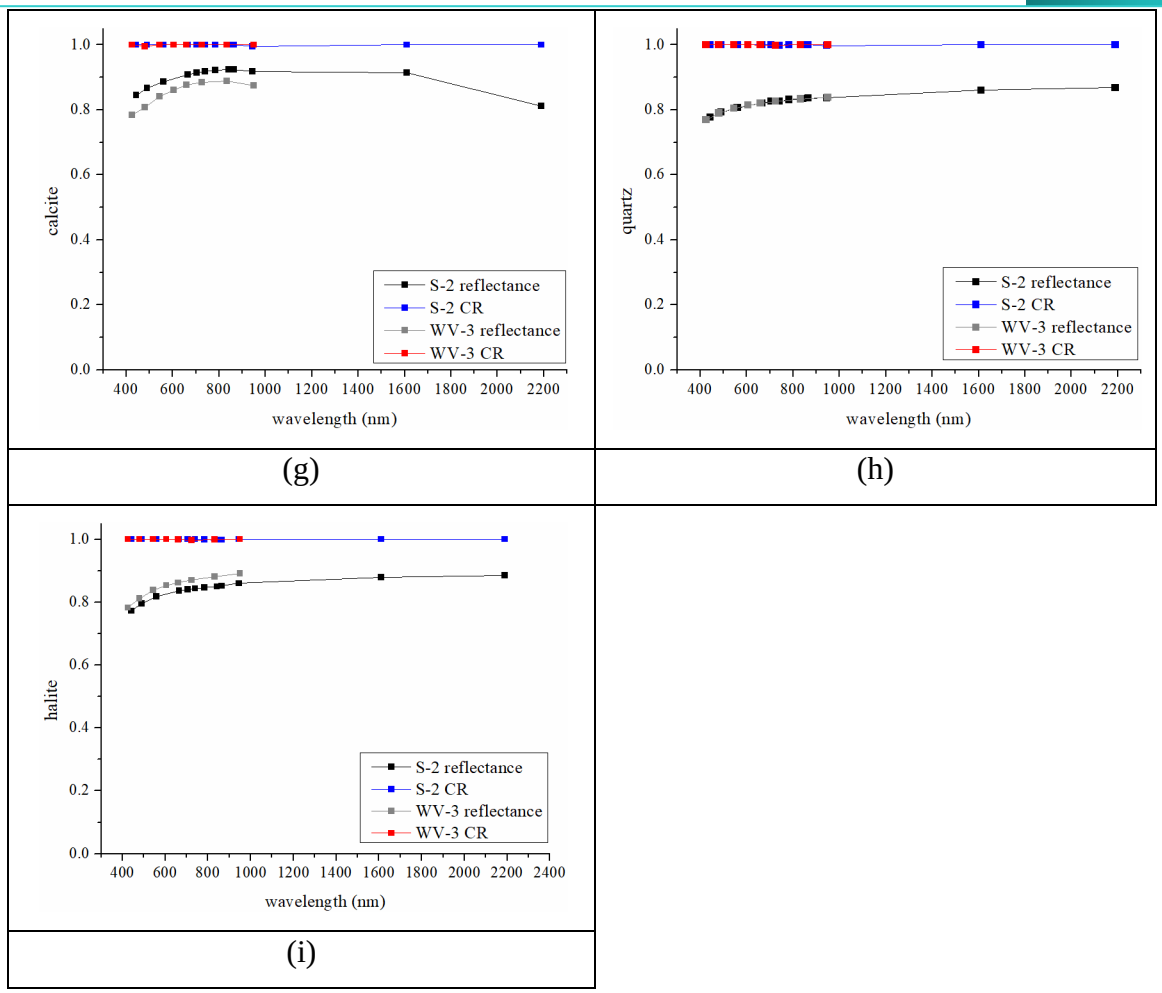

Fig. 7. Reflectance and CR reference spectral signatures of the minerals present in the study area. The spectral signatures that are retrieved from the USGS Spectral Library correspond to (a) goethite, (b) Mn_oxides/hydroxides, (c) muscovite (mica), (d) chlorite, (e) andesine (plagioclase), (f) orthoclase (K-feldspar), (g) calcite, (h) quartz and (i) halite; The reference spectral signature retrieved from PDS Geosciences Node Spectral Library corresponds to (b) manganite (Mn-oxides/hydroxides), All spectral signatures are resampled to S-2 (black and blue lines) and to WV-3 VNIR (gray and red lines) spectral bands; in black and gray: reflectance spectra; in red and blue: the corresponding CR spectra.

3.2.3 Processing of satellite data

Pre-processing

For notational simplification, hereafter, instead of writing, e.g., ‘‘band 1’’ and ‘‘band 2,’’ we write for S-2 data Sb1, *Sb*2, respectively and consequently, expressions like S*b*1/S*b*2 stand for the ratio of values in band *b*1 to values in band *b*2. A corresponding nomenclature is adopted for WV-3 VNIR spectral bands, namely W*b*1, W*b*2 etc. The main pre-processing steps of the satellite datasets are the following:

i. The WV-3 VNIR data are subset to the study area and atmospherically corrected. The atmospheric correction is performed on the subset image of the islet using the QUick Atmospheric Correction (QUAC) method in ENVI 5.5 image processing software (Bernstein et al., 2012).

ii. The S-2 Level 2A image is already atmospherically corrected. The reflectance image consists of 12 spectral bands, the wavelength centres of which are shown in Table 1. All spectral bands are resampled to 10 m spatial resolution. The S-2 image is subset to the study area and co-registered to the WV-3 VNIR image. The latter is performed due to the different zones in the UTM-WGS84 projection between the S-2 and WV-3 VNIR datasets.

Furthermore, due to differences in sea level around the islet between the two acquisition dates, an additional subsetting is performed, including sea masking, in order to retain only pixels on the surface of the islet that are exposed above sea level in both acquisition dates. Considering that sea level is higher on 15 January 2022 (WV-3 VNIR acquisition date) than on 17 July 2022 (S-2 acquisition date), a ROI (Region of Interest polygon) is created following the coastline in the WV-3 VNIR image and is used as mask. The difference in sea level between the two satellite acquisitions is spectrally evident from (i) the appearance of a reef on the sea surface southeast of the islet which is seen in the S-2 image and not in the WV-3 VNIR image, (b) when the two images are spectrally inspected in geographically linked views, the spectral signature of the coastal pixels above sea level on the islet in the S-2 image are submerged in the WV-3 VNIR image and (c) the spectral signature of the pixels on the sandy passage between the coast and the islet ("*tombolo*" in geomorphological terms) shows increased reflectance values in the blue-green bands in the S-2 image compared with the corresponding ones in the WV-3 VNIR image, indicating lower moisture content within the sand (Liu et al., 2002) (Fig. 8).

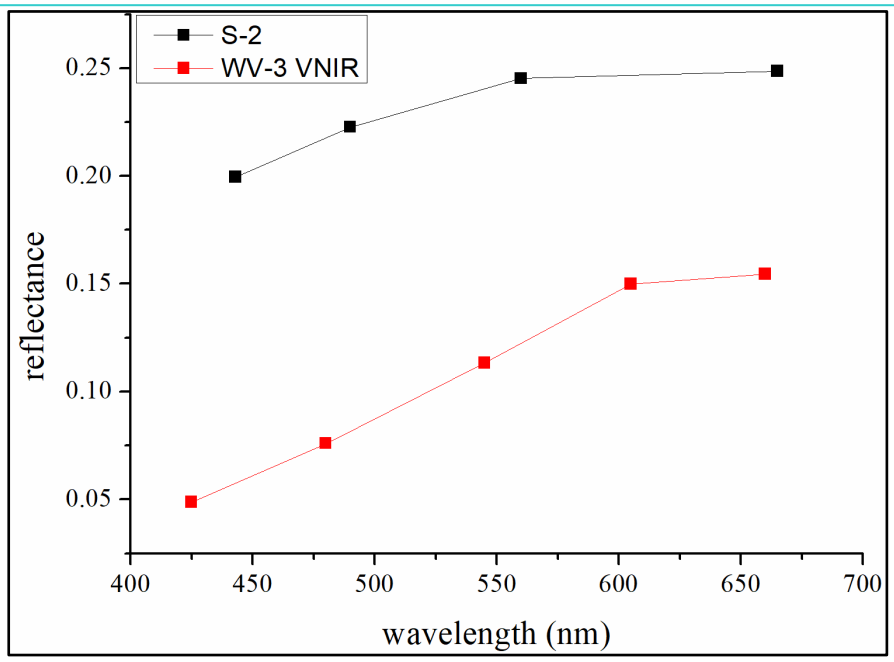

Fig. 8. Characteristic S-2 and WV-3 VNIR spectral signatures in the visible spectral bands of the sandy passage between the coast and the islet ("*tombolo*") pixels. The S-2 reflectance values are higher compared with the WV-3 VNIR corresponding ones, especially in the blue spectral area.

Main processing

The main processing consists of two procedures, one for the production of mineral maps (absorption maps) and one for the production of iron and alteration distribution maps (SI maps), A and B correspondingly in the flowchart in Fig. 5. Specifically:

a. Mineral maps

We first apply continuum removal to the satellite dataset which presents the best spectral/band configuration for the detection of the four Fe-Mn ore-related minerals, as it is resulted from the spectroscopy analysis on the reference mineral spectra. Then, for each band, for clarity purposes, we subtract each CR value from unity, creating thus the complementary pixel spectrum of the continuum removed one (named hereafter 1-CR) that corresponds to an absorption value. Absorption values in the 1-CR spectra range between 0 and 1, where 0 corresponds to no absorption and 1 to 100% absorption. The absorption maps at the diagnostic band/wavelength related to Fe-Mn ore related minerals are then extracted. In each map, pixels presenting an absorption value greater than 1% (0 indicates no absorption and 1 indicates full absorption) are mapped while pixels with absorption less than 1% are masked. The resulting absorption maps show the spatial distribution and corresponding absorption value of the specific mineral on the islet's surface.

b. SIs for iron bearing minerals and alteration

The production of SI maps of iron-bearing minerals and alteration is performed on the reflectance pixel spectra. The iron-bearing mineral maps are calculated separately, i.e., one map for ferric iron bearing minerals (goethite) and one map for ferrous iron bearing minerals (muscovite, chlorite). Most SIs are expressed in the form of simple band ratios and therefore, they are used to enhance the difference between a high reflectance and a diagnostic absorption feature in the spectral signature of the pixel under study. Between two bands of band numbers n and y (where $n>y$) in the image, the band ratio is defined as the ratio between their accociated values b_n and b_y, that is b_n/b_y. Consequently, an absorption feature is characterized as present when $b_n/b_y > 1$ and non-existent when $b_n/b_y \leq 1$ correspondingly. For each dataset, the SI is calculated on each reflectance pixel value according to their corresponding spectral bands position. In all SI maps, SI pixel values >1.01 are retained while SI pixel values <1.01 are masked. The SIs used in the study are described in detail here below.

— Ferric iron (Fe^{+3}) SI

The general formula for the calculation of the ferric iron-Fe^{+3} SI (Henrich et al., 2009) in terms of wavelength ranges (in nm) is expressed with Eq. 2; thus:

$$ferric\ iron = \frac{630:690}{520:600} \qquad \text{(Eq. 2)}$$

The calculation of the SI of ferric iron on S-2 data is expressed with Eq. 3 (modified from Van der Meer et al., 2014); thus:

$$SI_{Fe+3} = \frac{Sb4}{Sb2} \qquad \text{(Eq. 3)}$$

where, *Sb*4 and *Sb*2 are the corresponding *b*4 and *b*2 bands of S-2 data.
Correspondingly, the calculation of the SI of ferric iron on WV-3 VNIR data is indicated by Eq. 4 (SI online database):

$$SI_{Fe+3} = \frac{Wb5}{Wb3} \qquad \text{(Eq. 4)}$$

where, *Wb*5 and *Wb*3 are the corresponding *b*5 and *b*3 bands of WV-3 VNIR data.

It must be noted here that ferric iron SI is also indicative of the presence of Mn_oxides/hydroxides. This is due to the fact that, as it is the case of goethite, the ratio values S*b*4>S*b*2 and W*b*5/W*b*3 in the Mn_oxides/hydroxides spectrum are also >1 (Fig. 7a-b).

— Ferrous iron (Fe^{+2}) SI

The general formula for the calculation of the ferrous iron-Fe^{+2} SI (Rowan and Mars, 2003; Henrich et al., 2009) in terms of wavelength ranges (in nm) is expressed with Eq. 5; thus:

$$ferrous\ iron = \frac{2145:2185}{760:860} + \frac{520:600}{630:690} \qquad \text{Eq. (5)}$$

As seen in Eq. 5, the calculation involves the use of SWIR bands, therefore the ferrous SI can be calculated only using the S-2 spectral bands. The SI for ferrous iron for S-2 data is then calculated as expressed with Eq. 6 (Van der Meer et al., 2014); thus

$$SI_{Fe+2} = \frac{Sb12}{Sb8} + \frac{Sb3}{Sb4} \qquad \text{Eq. (6)}$$

where, S*b*3, S*b*4, S*b*8 and S*b*12 correspond to S-2 *b*3, *b*4, *b*8 and *b*12 spectral bands.

— Alteration SI

This specific index exploits the Al-OH absorption feature at 2200 nm and represents hydroxyl-bearing alteration minerals, especially clays (Hunt, 1979). The general formula for the calculation of the alteration SI (Hewson et al., 2001; Rowan and Mars, 2003; Henrich et al., 2009) in terms of wavelength ranges (in nm) is expressed with Eq. 7; thus:

$$SI_{alt} = \frac{1600:1700}{2145:2185} \qquad \text{Eq. (7)}$$

As in the case of the ferrous iron SI, the SWIR bands of the S-2 dataset allow the calculation of the alteration SI, as indicated by Eq. 8 (Van der Meer et al., 2014); thus

$$SI_{alt} = \frac{Sb11}{Sb12} \qquad \text{Eq. (8)}$$

where, S*b*11 and S*b*12 correspond to S-2 *b*11 and *b*12 spectral bands.

4. RESULTS AND DISCUSSION

4.1. Mineral diagnostic absorption features

Table 3 summarizes the absorption features of the nine minerals detected from XRD analysis and their corresponding maximum band depth (BD) values after the application of CR to their reflectance spectra (in both S-2 and WV-3 VNIR spectral bands) as shown in Fig. 7. The obtained results are presented and discussed here below:

– Plagioclase (andesine), quartz, K-feldspar (orthoclase), halite and calcite CR spectra are almost featureless in both S-2 and WV-3 VNIR spectral band configurations, therefore they cannot be detected by the spectral configurations of the two sensors (Fig. 7e-i, Table 3).

– Goethite: In the S-2 CR spectrum, goethite shows three characteristic ferric features. These absorption features are centred at 490 nm (S*b*2), 705 nm (S*b*5) and 945 nm (S*b*10), the first and the third being the strongest ones (Fig. 7a). The 705 nm (S*b*5) feature is weak. The 945 nm (S*b*10) feature is also observed in the mica and Mn_oxides/hydroxides spectral signatures and therefore, it cannot be considered as diagnostic of goethite. On the other hand, in the WV-3 VNIR spectral signature, goethite shows one strong absorption feature centred at 480 nm (W*b*2) and a secondary one at 660 nm (W*b*5). Both signatures are not observed in the other mineral spectra and therefore, they can both be considered diagnostic to goethite. However, the 660 nm (W*b*5) one is rather weak and could potentially be confused to a red absorption due to the presence of sparse vegetation within a pixel. Therefore, the diagnostic feature that characterizes goethite is 490 nm (S*b*2) in the S-2 bands and 480 nm (W*b*2) in the WV-3 VNIR bands (Table 3). It is interesting to note here, that the goethite diagnostic absorption in this spectral area is so strong that despite the 10 nm shift between S*b*2 and W*b*2 wavelength centres, it can be detected by both.

– Mn-oxides/hydroxides (manganite): In the S-2 CR spectrum, Mn-oxides/hydroxides show three strong features centred at 560 nm (S*b*3), 740 nm (S*b*6) and 865 nm (S*b*9) (Fig. 7b). However, the 740 nm (S*b*6) and 865 nm (S*b*9) ones are also observed within the signature of chlorite and therefore, they cannot be considered as diagnostic to Mn_oxides/hydroxides. On the other hand, the 560 nm (S*b*3) feature is not present within the other mineral spectra and thus, it can be considered as diagnostic. In the WV3 VNIR CR spectrum, Mn-ox/hydroxides show one feature centred at 605 nm (W*b*4) which is unique and hence, it can be used to differentiate Mn-ox/hydroxides

to the other minerals (Table 3). Overall, the diagnostic feature that characterizes Mn-oxides/hydroxides is 560 nm (S*b*3) in the S-2 bands and 605 nm (W*b*4) in the WV-3 VNIR bands (Table 3). It is interesting to note that, due to both sensors' spectral configurations, the centre wavelength of the WV-3 VNIR diagnostic feature is 40 nm longer than the S-2 corresponding one. However, the upper edge of the S*b*3 band width (542 nm - 578 nm) is less than 7 nm apart from the upper edge of the corresponding lower edge of the W*b*4 band width (585±5 - 625±5) and this explains why both spectral configurations can capture a feature within this area.

– Mica (muscovite): In its S-2 CR spectrum, mica shows two absorption features centred at 783 nm (S*b*7) and 945 nm (S*b*10). The 783 nm (S*b*7) feature seems to be present only in the mica spectrum and thus it can be considered as diagnostic to mica (Fig. 7c). On the other hand, the 945 nm (S*b*10) feature is also observed in andesine, Mn oxides/hydroxides and goethite spectra. In the case of the WV-3 VNIR mica spectrum, there is one absorption feature that is centred at 725 nm (W*b*6) which is also observed within the corresponding chlorite spectrum. Therefore, it seems that mica can be differentiated only with the S-2 spectral band configuration and not with the WV-3 VNIR corresponding one.

– Chlorite: In its S-2 CR spectrum, chlorite shows a unique feature centred at 865 nm (S*b*9) which is present only in the chlorite spectrum and therefore, differentiates chlorite from all the other minerals (Fig. 7d). On the other hand, in its WV-3 VNIR CR spectrum, chlorite shows one feature centred at 725 nm (W*b*6) which is also observed within the mica spectrum. Therefore, it seems that chlorite can be differentiated only with the S-2 spectral bands and not with the WV-3 VNIR spectral band configuration. We note that in its original reference spectrum, chlorite shows two weak absorption features centred on 715 nm and 887 nm. The 715 nm one is captured by W*b*6 (725 nm) due to its band width (685 nm - 765 nm) which includes the centre of the absorption feature (715 nm). In parallel, this feature is not captured by S*b*5 (705 nm) because it is not included within its band width (~697 nm - ~713 nm), despite the fact that it is only 2 nm outside of the band upper edge. This is also the case of S*b*6 (740 nm) with a band width between ~732 nm and ~748 nm. The above findings explain why the 715 nm absorption can be captured by W*b*6 and not by any S-2 band. Concerning the second weak chlorite absorption (887 nm), S*b*9 (865 nm) can capture this feature because the upper edge of the band (~856 nm - ~876 nm) is only 11 nm shorter than the centre of the 887nm absorption.

Table 3. Band/wavelength position and corresponding Band depths (BDs) of mineral absorption features in (a) S-2 and (b) WV3 VNIR CR spectra of the nine minerals detected in the study area, namely qz: quartz, cal: calcite, plg: plagioclase (andesine), mica (muscovite), chl: chlorite, Mn-ox/hydrox: Mn-oxides/hydroxides, fsp: K-feldspar (orthoclase), goe: goethite, hal: halite. In gray: features with BD< 1%, in orange: the diagnostic absorption feature that differentiates the mineral from the other minerals, in yellow: all features with BD>1%.

(a) S-2 spectral bands										
band	centre wavelength (nm)	qz	cal	plg	micas	chl	Mn-Ox/hydrox	fsp	goe	hal
1	443									
2	490								0.656	
3	560						0.670			
4	665									
5	705			0.997					0.949	
6	740	0.998				0.719	0.692			
7	783				0.909					
8	842	0.999		0.988				0.999		0.998
9	865					0.679				
10	945	0.997	0.994	0.987	0.662		0.656		0.6156	
11	1610							0.992		
12	2190									
(b) WV-3 VNIR spectral bands										
band	centre wavelength (nm)	qz	cal	plg	mica	chl	Mn-Ox/hydrox	fsp	goe	hal
1	425									
2	480		0.995	0.990					0.52	
3	545									
4	605						0.469			
5	660								0.916	0.998
6	725	0.999			0.962	0.887		0.9991		0.997
7	832.5			0.991						0.999
8	950									

Overall, the spectroscopy analysis on the reference CR spectra shows that ferric oxides (goethite) and Mn-oxides/hydroxides (manganite) can be detected, differentiated and mapped in the spectral configurations of both satellite sensors. On the other hand, ferrous-iron bearing minerals, namely mica (muscovite) and chlorite (clinochlore), can be spectrally distinguished only in the S-2 spectral bands. Furthermore, non iron-bearing minerals, namely quartz, calcite, halite and K-feldspar are spectrally featureless in both S-2 and WV-3 VNIR spectral band configurations and thus they cannot be detected and mapped. Concluding, all four minerals that could be related to Fe-Mn mineralization (goethite, Mn-oxides/hydroxides, mica and chlorite) can be detected and mapped with the S-2 spectral bands. Table 4 summarizes the above findings.

Table 4. Centre wavelength and corresponding band number (in S-2 and WV-3 VNIR spectral configurations) of the diagnostic absorption feature(s) of the minerals that could be related to Fe-Mn ore.

Mineral	S-2 band centre (nm)	WV-3 VNIR band centre (nm)
Goethite	490nm (S*b*2)	480nm (W*b*2) 660nm (W*b*5)
Mn-oxides/hydroxides	560nm (S*b*3)	605nm (W*b*4)
Mica	783nm (S*b*7)	-
Chlorite	865nm (S*b*9)	-

4.2 Mineral absorption feature maps

The absorption maps that correspond to the four Fe-Mn ore related minerals are presented in Fig. 9. The maps are produced using the S-2 dataset which, according to the previous spectroscopy analysis (see section 4.1), is the one that can distinguish all four minerals (Table 4).

From the maps showing the spatial distribution of the four minerals (Fig. 9), one can observe that there is significant mineralization related to the igneous intrusion on the islet. The hydrothermal alteration is observed on the entire islet surface, on both schists and granitoid but to a different degree. It seems that all four minerals show high values at the centre of the eastern part of the islet indicating that the alteration seems to be stronger where the granitoid/schist contact is located. Especially concerning Mn_oxides/hydroxides, they seem to be present mainly at the eastern part of the islet (Fig. 9b). Goethite and chlorite seem to show the highest spatial distribution in terms of high absorption values (Fig. 9a, d). The muscovite highest absorption values are almost exclusively observed at the eastern part of the islet (Fig. 9c) compared to the chlorite corresponding ones which seem to be relatively more uniformly distributed on the islet (Fig. 9d)

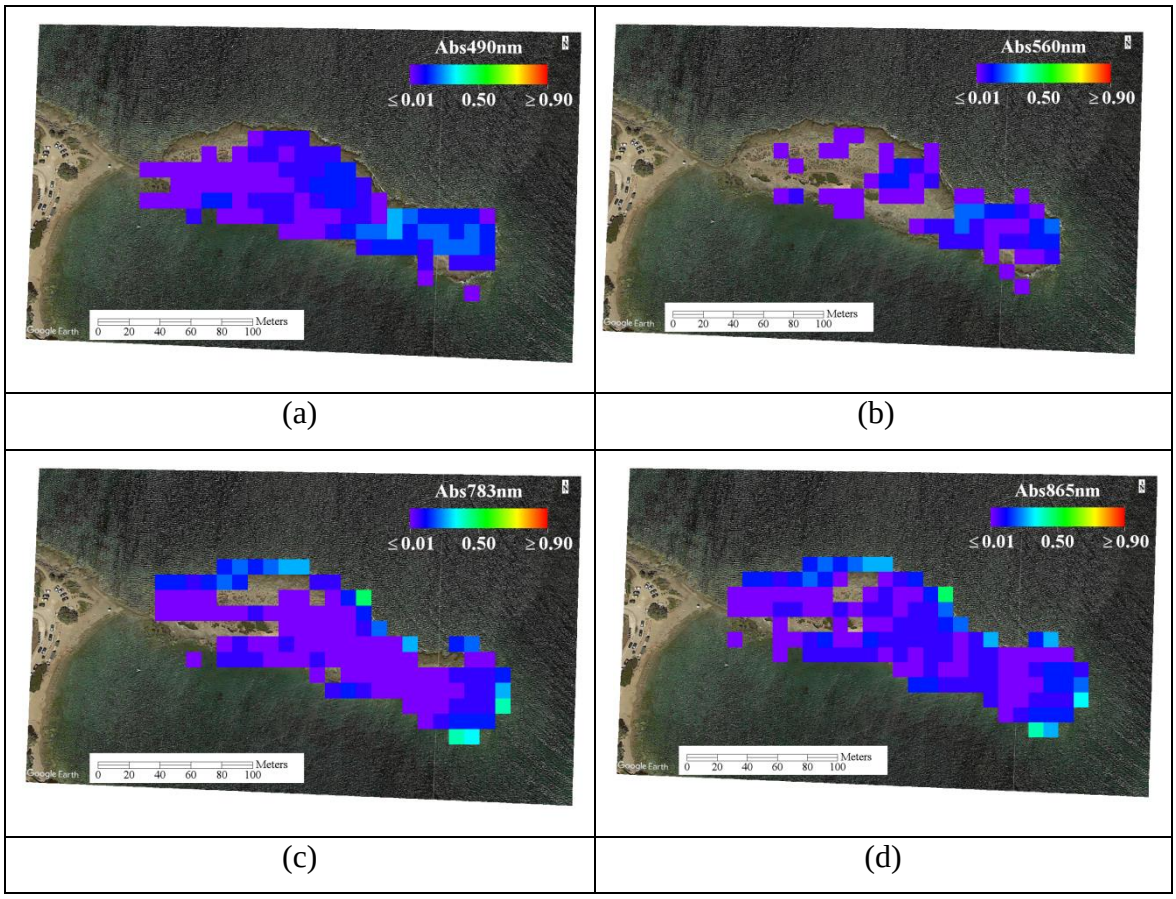

Fig. 9. Mineral absorption maps issued from the S-2 satellite image. (a) absorption map centred at 490 nm, corresponding to goethite; (b) absorption map centred at 560 nm, corresponding to Mn-oxides/hydroxides; (c) absorption map centred at 783 nm, corresponding to muscovite; (d) absorption map centred at 865 nm, corresponding to chlorite. The background image is a Google Earth image, co-registered to the WV-3 VNIR image. Absorption values <1% are masked.

4.3 SI maps

The SI maps of ferric iron, ferrous iron and alteration are shown in Fig. 10. The spectral band configuration of S-2, including both VNIR and SWIR bands, allows the calculation of both ferric and ferrous iron SIs as well as the alteration SI while the spectral configuration of WV-2 VNIR only allows the calculation of ferric iron SI. It must be reminded here, that the ferric iron SI indicates the presence of both goethite and Mn_oxides/hydroxides.

Both S-2 and WV-3 VNIR ferric iron maps (Fig. 10a-b) show a strong presence of goethite and Mn_oxides/hydroxides at the eastern part of the islet where the contact with the granitoid is located. However, ferric iron presence is observed on the entire surface of the islet, especially in the S-2 ferric map (Fig. 10a). The differences in the SI values between S-2 and WV-3 VNIR pixels are due to (i) the differences in the wavelength centres of the bands used in the calculation of the SI and (b) the different

spatial resolution between the two datasets. As it is the case of ferric iron, ferrous iron (corresponding to muscovite and chlorite) is also observed on the entire surface of the islet but with different values (Fig. 10c-d). Generally, both ferric and ferrous iron bearing minerals are present on the entire surface islet indicating that hydrothermal alteration affects both the schists and the granitoid. This is consistent with the alteration SI map (Fig. 10d) which shows that the highest values are observed at the eastern part of the islet. We note that the SI alteration values are most probably indicative of the degree of alteration according to the results of a similar study presented by Tompolidi et al. (2020) on the hydrothermal field of Nisyros volcano (Greece).

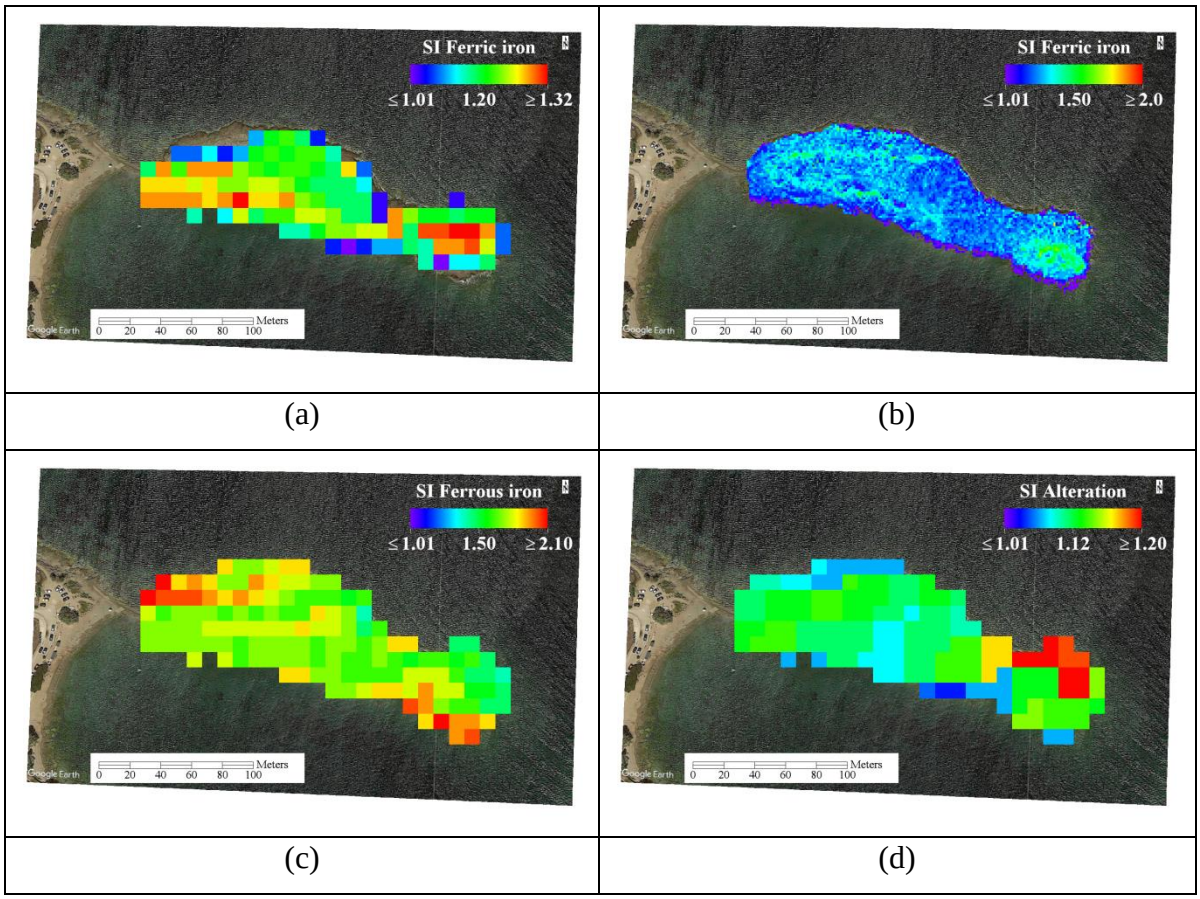

Fig. 10. SI maps. (a) Ferric iron SI map calculated on the S-2 image; (b) Ferric iron SI map calculated on the WV-3 VNIR image; (c) Ferrous iron SI map calculated on the S-2 image; (d) Hydroxyl-alteration map calculated on the S-2 image. All maps show that ferric iron, ferrous iron and alteration are present, to a higher or lesser degree, on the entire surface of the islet. The background image is a Google Earth high resolution image, co-registered to the WV-3 VNIR image. SI values ≤ 1.01 are masked (in band ratios values ≤1 indicate that the material does not exist).

Concluding, the results of both approaches, reflectance spectroscopy and SI mapping, are consistent. Hydrothermal alteration seems to be present on the entire surface of the

islet, both on the schists and the granitoid (Fig. 10d). The strongest alteration seems to be observed at the eastern part of the islet. Ferric iron is also present on the entire surface of the islet (Fig. 10a-b), and in particular, at the eastern part of the islet where the highest values of goethite and Mn_oxides/hydroxides are observed (Fig. 9a-b). Concerning the distribution of ferrous iron (Fig. 10c), it is present on the entire surface of the islet, with the highest values observed at the south-eastern part. Concerning the two ferrous iron-bearing minerals, the spatial distribution of chlorite is more homogenous on the entire islet while the presence of muscovite seems to be higher at the eastern part of the islet (Fig. 9c).

This study has shown that Fe-Mn ore related minerals are present on the islet and laboratory and satellite data analyses results are consistent and complementary. Despite its high spatial resolution, WV-3 VNIR is only sensitive to the ferric phases (ferric absorption bands occur at wavelengths shorter than 900 nm, depending on mineralogy and chemical composition) due to its rather low spectral resolution and wavelength range till 950 nm. It must be noted that the ferrous iron absorption band is usually centred near 1 μm but varies between 900 nm and 1400 nm depending on both mineralogy and chemical composition; a second absorption band is usually centred near 2 μm but varies between 1800 and 2400 nm (Bishop and Murad, 1996; Cloutis et al., 2006). On the other hand, S-2 with its higher spectral resolution (including additional VNIR bands and two SWIR bands) can detect hydroxyl-bearing alteration and map zones exhibiting both ferric and ferrous-bearing alteration minerals that are potentially linked to Fe-Mn ore. However, additional sampling and laboratory analyses are required in order to spatially validate the produced mineral maps and to investigate potential relations between mineral concentrations and absorption magnitudes obtained from the satellite data.

5. CONCLUSIONS

In this paper, we present the findings of a joint remote sensing and laboratory examination of a mineralization zone induced by the intrusion of an igneous body onshore the islet of “Koutala”, in Lavreotiki, Greece. Our objective was to investigate the potential of S-2 and WV-3 VNIR data to detect and map alteration minerals which are detected from laboratory analysis of samples and could be linked to Fe-Mn ore. Laboratory analyses have detected four minerals that could be linked to Fe-Mn ore, namely goethite, Mn_oxides/hydroxides, micas and chlorite. Two methods were applied, namely reflectance spectroscopy and spectral indices. The resulting mineral

maps have shown that laboratory and both satellite data analyses results are consistent and complementary.

Moreover, despite its very high spatial resolution and due to its low spectral resolution (including its spectral range), the V-3 VNIR dataset seems to be only sensitive to the presence of ferric iron and Mn_oxides/hydroxides. On the other hand, S-2 seems to be capable to detect and map zones exhibiting all four alteration minerals potentially linked to Fe-Mn-ore. The produced mineral maps show that there is significant mineralization related to the granitoid. Hydrothermal alteration, to a different degree, is observed on the entire islet surface (on both schists and granitoid). However, alteration seems to be stronger at the eastern part of the islet where the granitoid/schist contact is located. Additional sampling and laboratory analyses are foreseen in order to spatially validate the produced mineral distribution maps as well as to investigate potential relations between mineral concentrations and absorption/SI value magnitudes issued from the satellite data.

6. DATA AVAILABILITY

Sentinel-2 data are freely available for downloading through ESA's Sentinel-2 data hub. Worldview-3 VNIR data are commercially distributed.

7. CONFLICTS OF INTEREST

The authors declare that they have no conflict of interest regarding this publication.

8. FUNDING STATEMENT

The authors received no financial support for this research.

9. ACKNOWLEDGEMENTS

We would like to thank Vana Giavi for making available the Worldview-3 data and Panagiotis Grigorakakis for his help with the GNSS data acquisition. We were motivated to study this area after a field trip organized by the Geological Society of Greece on 2 July 2022.

10. REFERENCES

Abrams, M., Brown, D., Lepley, L., Sadowski, R., 1983. Remote sensing of porphyry copper deposits in Southern Arizona. *Economic Geology*, 78, 4, 591–604. https://doi.org/10.2113/gsecongeo.78.4.591

Abrams, M., Hook, S.J., 1995. Simulated ASTER Data for Geological Studies. *IEEE Transaction on Geo-science and Remote Sensing*, 33, 692-699. https://doi.org/10.1109/36.387584

Abrams, M., Tsu, H., Hulley, G., Iwao, K., Pieri, D., Cudahy, T., Kargel, J., 2015. The advanced spaceborne thermal emission and reflection radiometer (ASTER) after fifteen years: Review of global products. *International Journal of Applied Earth Observation and Geoinformation*, 38, 292–301. https://doi.org/10.1016/j.jag.2015.01.013

Abubakar, A.J.A., Hashim, M., Pour, A.B., 2019. Identification of hydrothermal alteration minerals associated with geothermal system using ASTER and Hyperion satellite data: A case study from Yankari Park, NE Nigeria. *Geocarto International*, 34, 597–625, https://doi.org/10.1080/10106049.2017.1421716

Adiri, Z., Lhissou, R., El Harti, A., Jellouli, A., & Chakouri, M., 2020. Recent advances in the use of public domain satellite imagery for mineral exploration: A review of Landsat-8 and Sentinel-2 applications. *Ore Geology Reviews*, 117, 103332. https://doi.org/10.1016/j.oregeorev.2020.103332

Altherr, R., Kreuzer, H., Wendt, I., Lenz, H., Wagner, G.A. Keller, J., Harre, W., Hohndorf, A., 1982. A late Oligocene/early Miocene high temperature belt in the Attic-Cycladic crystalline complex (SE Pelagonian, Greece). *Geol. Jahrb*., E23, 97 – 164.

Anifadi, A., Parcharidis, I., Sykioti, O., 2016. Hydrothermal alteration zones detection in Limnos Island, through the application of Remote Sensing. Proceedings of the 14th International Conference of the Geological Society of Greece, *Bulletin of the Geological Society of Greece*, 50(3). https://doi.org/10.12681/bgsg.11879

Anifadi, A., Sykioti, O., Koutroumbas, K., Vassilakis, E., 2022. A Novel Spectral Index for Identifying Ferronickel (Fe–Ni) Laterites from Sentinel 2 Satellite Data, *Natural Resources Research*, 31, 198, https://doi.org/10.1007/s11053-022-10055-6

Askari. G., Pour, A.B., Pradhan, B., Sarfi, M., Nazemjehad, F., 2018. Band Ratios Matrix Transformation (BRMT): A Sedimentary Lithology Mapping Approach Using ASTER Satellite Sensor. *Sensors*, 18(10), 3213. https://doi.org/10.3390/s18103213

Berger, A., Schneider, D., Grasemann, B., Stockli, D., 2012. Footwall mineralization during Late Miocene extension along the West Cycladic Detachment System, Lavrion, Greece. *Terra Nova*, 25(3), 181-191, https://doi.org/10.1111/ter.12016

Bishop, JL, Murad E., 2005. The visible and infrared spectral properties of jarosite and alunite. *American Mineralogist*, 90, 1100–1107. https://doi.org/10.2138/am.2005.1700

Bonsall, T.A., Spry, P.G., Voudouris, P., St. Seymour, K., Tombros, S., Melfos, V., 2007. Fluid inclusion and stable isotope characteristics of carbonate replacement Pb-Zn-Ag deposits in the Lavrion district, Greece. In Mineral exploration and research: Digging deeper, Andrews, C.J., et al., Eds. *Irish Association for Economic Geology*: Dublin, Ireland, pp. 283-286.

Burns, R. G., 1993. Mineralogical applications of crystal field theory. 2nd Ed. Cambridge University Press. https://doi.org/10.1017/CBO9780511524899

Clark, R. N., Roush, T. L., 1984. Reflectance spectroscopy—quantitative analysis techniques for remote sensing applications. *Journal of Geophysical Research*, 89, 6329–6340. https://doi.org/10.1029/JB089iB07p06329

Clark, R., 1999. Spectroscopy of Rocks and Minerals, and Principles of Spectroscopy, In Remote Sensing for the Earth Sciences: Manual of Remote Sensing, 3rd Ed., Rencz, A.M., Ed. Wiley: New York, NY, USA, Ch. 1; Vol. 3, 728p.

Cloutis, E. A., 1996. Review article hyperspectral geological remote sensing: Evaluation of analytical techniques. *International Journal of Remote Sensing*, 17, 12, 2215–2242. https://doi.org/10.1080/01431169608948770

Cudahy, T., Hewson, R., 2002. ASTER geological case histories: porphyry-skarnepithermal, iron oxide Cu-Au and Broken hill Pb-Zn-Ag. *Annual General Meeting of the Geological Remote Sensing Group 'ASTER Unveiled'*, Burlington House, Piccadilly, London, UK.

DigitalGlobe Inc., 2017. Data sheet for WorldView 3 available online in https://dg-cms-uploads-production.s3.amazonaws.com/uploads/document/file/95/DG2017_WorldView-3_DS.pdf

Economou, M., Skounakis, S., Papathanasiou, C., 1981. Magnetite deposits of skarn type from the Plaka area of Laurium, Greece. *Chemie der Erde*, 40, 241−252, ISSN: 0009-2819.

El Kati, I., Nakhcha, C., El Bakhchouch, O., Tabyaoui, H., 2018. Application of ASTER and Sentinel-2A Images for geological mapping in arid regions: The Safsafate Area in the Neogen Guercif basin, Northern Morocco, *International Journal of Advances in Remote Sensing GIS*, 7, 2782–2792. https://doi.org/10.23953/cloud.ijarsg.374

Farmer, V.C., 1974. The Infrared Spectra of Minerals. Mineralogical Society, London, UK, 539p.

Ferrier, G., White, K., Griffiths, G., Bryant, R., Stefouli, M., 2010. The mapping of hydrothermal alteration zones on the island of Lesvos, Greece using an integrated remote sensing dataset. *International Journal of Remote Sensing*, 23, 2, 341-356. https://doi.org/10.1080/01431160010003857

Ferrier, G.; Naden, J.; Ganas, A.; Kemp, S.; Pope, R. 2016. Identification of Multi-Style Hydrothermal Alteration Using Integrated Compositional and Topographic Remote Sensing Datasets. Geosciences, 6 (3), 36 doi:10.3390/geosciences6030036. http://www.mdpi.com/2076-3263/6/3/36/html

Ferrier, G., Pope, R., Ganas, A., 2019. Prospectivity mapping for high sulfidation epithermal porphyry deposits using an integrated compositional and topographic remote sensing dataset. *Ore Geology Reviews*, 107, 353-363. https://doi.org/10.1016/j.oregeorev.2019.02.029

Gad, S., Kusky, T., 2007. ASTER spectral ratioing for lithological mapping in the Arabian–Nubian shield, the Neoproterozoic Wadi Kid area, Sinai, Egypt. *Gondwana Research*, 11, 326–335. https://doi.org/10.1016/j.gr.2006.02.010

Ganas A., and Ferrier, G., 2002. Mapping epithermal gold in Milos using DAIS Hyperspectral data. ΟΡΥΚΤΟΣ ΠΛΟΥΤΟΣ (in Greek with English Summary), Mineral Wealth, 122, 37-46.

Ge, W., Cheng, Q., Tang, Y., Jing, L., Gao, C., 2018(a). Lithological classification using Sentinel-2A data in the Shibanjing ophiolite complex in Inner Mongolia, China. *Remote Sensing*, 10, 638. https://doi.org/10.3390/rs10040638

Ge, W., Cheng, Q., Jing, L., Armenakis, C., Ding, H., 2018(b). Lithological discrimination using ASTER and Sentinel-2A in the Shibanjing ophiolite complex of Beishan orogenic in Inner Mongolia, China. *Advanced Space Research*, 62, 1702–1716. https://doi.org/10.1016/j.asr.2018.06.036

Goetz, A. F. H., Rowan, L. C., 1981. Geologic remote-sensing. *Science*, 211, 4484, 781–791. https://doi.org/10.1126/science.211.4484.781

Henrich, V., Götze, C., Jung, A., Sandow, C., Thürkow, D., Glaesser, C., 2009. Development of an online indices database: Motivation, concept and implementation. *6th EARSeL Imaging Spectroscopy SIG Workshop Innovative Tool for Scientific and Commercial Environment Applications*, Tel Aviv, Israel.

Hewson, R.D., Cudahy, T.J., Huntington, J.F., 2001. Geologic and alteration mapping at Mt Fitton, South Australia, using ASTER satellite-borne data. *Geoscience and Remote Sensing Symposium, IGARSS '01. IEEE 2001 International*, 2, 724-726. https://doi.org/10.1109/igarss.2001.976615

Hosseinjani, M., Tangestani, M.H., 2011. Mapping alteration minerals using sub-pixel unmixing of ASTER data in the Sarduiyeh area, SE Kerman, Iran. *International Journal of Digital Earth*, 4, 487–504. https://doi.org/10.1080/17538947.2010.550937

Hu, B., Xu, Y., Wan, B., Wu, X., Yi, G., 2018. Hydrothermally altered mineral mapping using synthetic application of Sentinel-2A MSI, ASTER and Hyperion data in the Duolong area, Tibetan. *Ore Geology Reviews*, 101, 384–397. https://doi.org/10.1016/j.oregeorev.2018.07.017

Hunt, G. R., 1977. Spectral signatures of particulate minerals in the visible and near infrared. *Geophysics*, 42, 3, 501–513. https://doi.org/10.1190/1.1440721

Hunt, G. R., Ashley, R. P., 1979. Spectra of altered rocks in the visible and near infrared. *Economic Geology*, 74, 7, 1613–1629. https://doi.org/10.2113/gsecongeo.74.7.1613

Jackson, R. D., 1983. Spectral Indices in N-Space. *Remote Sensing of Environment*, 13, 5, 409–421. https://doi.org/10.1016/0034-4257(83)90010-X

Kalinowski, A., Oliver, S., 2004. ASTER Mineral Index Processing Manual. In: Remote Sensing Applications Geoscience Australia. (available online in https://www.ga.gov.au/webtemp/image_cache/GA7833.pdf).

Kruse, F.A., 2010. Mineral mapping using spectroscopy: from field measurements to airborne and satellite-based spectrometry. *ASARS Symposium Boulder, Colorado, USA*, p. 1-15.

Kruse, F.A., 2012. Mapping surface mineralogy using imaging spectrometry. *Geomorphology*, 137, 1, 41-56. https://doi.org/10.1016/j.geomorph.2010.09.032

Kruse, F.A., 1988. Use of airborne imaging spectrometer data to map minerals associated with hydrothermally altered rocks in the northern Grapevine Mountains, Nevada, and California. *Remote Sensing of Environment*, 24, 1, 31–51. https://doi.org/10.1016/0034-4257(88)90004-1

Lanfranchi, R.A., Cerqueira, Pereira Cruz, S., Rocha, F., 2021. Application of remote sensing and reflectance spectroscopy to explore iron-enriched domains in the north region of the intracontinental sector of the Aracuai West Congo Orogen. *Ore Geology Reviews*, 128, 103916. https://doi.org/10.1016/j.oregeorev.2020.103916

Liu, W., Baret, F., Xinfa, G., Qingxi, T., Lanfen, Z., Bing, Z., 2002. Relating soil surface moisture to reflectance. *Remote Sensing of Environment*, 81(2-3), 238-246. https://doi.org/10.1016/S0034-4257(01)00347-9

Marinos, G., Petrascheck, W.E., 1956. Laurium: Geological and geophysical research. Greece. Institute for Geology and Subsurface Research, 4, 1–246.

Mars, J.C., Rowan, L.C., 2010. Spectral assessment of new ASTER SWIR surface reflectance data products for spectroscopic mapping of rocks and minerals. *Remote Sensing of Environment*, 114, 2011–2025. https://doi.org/10.1016/j.rse.2010.04.008

Mekik, C, Arslanoglu, M., 2009. Investigation on Accuracies of Real Time Kinematic GPS for GIS Applications. *Remote Sensing*, 1, 1, 22-35. https://doi.org/10.3390/rs1010022

Mielke, C., Bösche, N.K., Rogass, C., Segl, K., Gauert, C., Kaufmann, H., 2014. Potential applications of the Sentinel-2 multispectral sensor and the EnMap hyperspectral sensor in mineral exploration. *Earsel Eproceedings*, 13, 93–102. https://doi.org/10.12760/01-2014-2-07

Nikolakopoulos, G.K., Vaiopoulos, D.A., Skianis, G.A., 2007. A preliminary approach on the use of satellite hyperspectral data for geological mapping. Proceedings of the 11th International Congress of the Geological Society of Greece, *Bulletin of the Geological Society of Greece*, 40, 1998-2007. https://doi.org/10.12681/bgsg.17251

Nikolakopoulos, K., Gioti, E., Skianis, G., Vaiopoulos, D., 2010. Ameliorating the spatial resolution of Hyperion hyperspectral data. The case of Antiparos island. Proceedings of the 12th International Congress of the Geological Society of Greece, *Bulletin of the Geological Society of Greece*, 43(3), 1627-1636. https://doi.org/10.12681/bgsg.11337

Nikolakopoulos, G.K., Lampropoulou, P., Papoulis, D., Rogkala, A., Giannakopoulou, P.P., Petrounias, P., 2018. Combined use of Remote Sensing Data, Mineralogical Analyses,

Microstructure Studies, and Geographic Information System for Geological Mapping of Antiparos Island (Greece). *Geosciences*, 8(3), 96. https://doi.org/10.3390/geosciences8030096

Ninomiya Y, Fu, B., 2019. Thermal infrared multispectral remote sensing of lithology and mineralogy based on spectral properties of materials. *Ore Geology Reviews*, 108, 54–72. https://doi.org/10.1016/j.oregeorev.2018.03.012

Oikonomidis, D., Vavelidis, Melfos, V., Artashova, M., 2016. Searching for ancient gold mines in Filippoi area, Macedonia, Greece, using Worldview-2 satellite imagery. *Geocarto International*, 87-96. http://dx.doi.org/10.1080/10106049.2015.1128487

Papanikolaou, D.J., Syskakis, D., 1991. Geometry of acid intrusives in Plaka, Laurium and relation between magmatism and deformation. *Bulletin of the Geological Society of Greece*, 25, 355-368.

Park, H., Choi, J., 2021. Mineral Detection Using Sharpened VNIR and SWIR Bands of Worldview-3 Satellite Imagery. *Sustainability*, 13, 5518. https://doi.org/10.3390/su13105518

Pe-Piper, G., Piper, D., 2002. The igneous rocks of Greece: anatomy of an orogen, 1st ed.; Beiträge zur Regionalen Geologie der Erde: Stuttgart, Germany, 588 p., ISBN 978-3-443-11030-7.

Photiades, A., Carras, N., 2001. Stratigraphy and geological structure of the Lavrion area (Attica, Greece). *Bulletin of the Geological Society of Greece*, 34, 103-109.

Pour, A.B., Hashim, M.; Marghany, M., 2011. Using spectral mapping techniques on short wave infrared bands of ASTER remote sensing data for alteration mineral mapping in SE Iran. *International. Journal of Physical Sciences*, *6*, 917–929. https://doi.org/10.5897/IJPS10.510

Pour, A.B., Hashim, M., Hong, J.K., Park, Y., 2019. Lithological and alteration mineral mapping in poorly exposed lithologies using Landsat-8 and ASTER satellite data: North-eastern Graham Land, Antarctic Peninsula. *Ore Geology Reviews*, 108, 112–133, https://doi.org/10.1016/j.oregeorev.2017.07.018

Purwadi, I., van der Werff, H., Lievens, C., 2020. Targeting rare earth element bearing mine tailings on Bangka Island, Indonesia, with Sentinel-2 MSI. *International Journal of Applied Earth Observation and Geoinformation*, 88, 102055. https://doi.org/10.1016/j.jag.2020.102055

Rajendran, S., Thirunavukkarasu, A., Balamurugan, G., Shankar, K., 2011. Discrimination of iron ore deposits of granulite terrain of Southern Peninsular India using ASTER data. *Journal of Asian Earth Sciences*, 41, 99–106. https://doi.org/10.1016/j.jseaes.2011.01.004

Rajendran, S., 2017. Characterization of ASTER spectral bands for mapping alteration zones of volcanic massive sulphide deposits. *Ore Geology Reviews*, 88, 317–335. https://doi.org/10.1016/j.oregeorev.2017.04.016

Rowan, L. C., Mars, J. C., 2003. Lithologic mapping in the mountain pass, California area using advanced spaceborne thermal emission and reflection radiometer (ASTER) data. *Remote Sensing of Environment*, 84, 350–366. https://doi.org/10.1016/S0034-4257(02)00127-X

Rowan, L.C., Schmidt, R.G., Mars, J.C., 2016. Distribution of hydrothermally altered rocks in the Reko Diq, Pakistan mineralized area based on spectral analysis of ASTER data, *Remote Sensing of Environment*, 104, 1, 74-87. https://doi.org/10.1016/j.rse.2006.05.014

Sabins, F. F., 1999. Remote sensing for mineral exploration. *Ore Geology Reviews*, 14, 157–183. https://doi.org/10.1016/S0169-1368(99)00007-4

Salehi, T., H. Tangestani, M., 2020. Evaluation of WorldView-3 VNIR and SWIR Data for Hydrothermal Alteration Mapping for Mineral Exploration: Case Study from Northeastern Isfahan, Iran. *Natural Resources Research*, 29, 3479–3503. https://doi.org/10.1007/s11053-020-09703-6

Scheffer, C., Vanderhaeghe, O., Lanari, P., Tarantola, A., Ponthus, L., Photiades, A., France, L., 2016. Syn- to post-orogenic exhumation of metamorphic nappes: Structure and thermobarometry of the western Attic-Cycladic metamorphic complex (Lavrion, Greece). *Journal of Geodynamics*, 96, 174 – 193. https://doi.org/10.1016/j.jog.2015.08.005

Shim, K., Yu, J., Wang, L., Lee, S., Koh. S-M., Lee, B.H., 2021. Content Controlled Spectral Indices for Detection of Hydrothermal Alteration Minerals Based on Machine Learning and Lasso-Logistic Regression Analysis. *IEEE Journal of Selected Topics in Applied Earth Observations and Remote Sensing*, 14, 7435-7447. https://doi.org/10.1109/JSTARS.2021.3095926

Shuai, S., Zhang, Z., Lv, X. et al., 2022. Assessment of new spectral indices and multi-seasonal ASTER data for gypsum mapping. *Carbonates Evaporites*, 37, 34. https://doi.org/10.1007/s13146-022-00775-4

Skarpelis, N., 2002. Geodynamics and evolution of the Miocene mineralization in the Cycladic-Pelagonian Belt, Hellenides. *Bulletin of the Geological Society of Greece*, 34, 2191-2209.

Skarpelis, N., Tsikouras, B., Pe-Piper, G., 2007. The Miocene igneous rocks in the Basal unit of Lavrion (SE Attica, Greece): Petrology and geodynamic implications. *Geological Magazine*, 145, 1–15. https://doi.org/10.1017/S0016756807003949

Skarpelis, N., Argyraki, A., 2008. Geology and origin of supergene ore at the Lavrion Pb-Ag-Zn deposit, Attica, Greece. *Resource Geol*ogy, 59, 1-14. https://doi.org/10.1111/j.1751-3928.2008.00076.x

Soydan, H., Koz, A., Duzgun, H.S., 2021. Secondary iron mineral detection via hyperspectral unmixing analysis with sentinel-2 imagery. *International Journal of Applied Earth Observation and Geoinformation*, 101, 102343. https://doi.org/10.1016/j.jag.2021.102343

Sun, Y., Tian, S., Di, B., 2017. Extracting mineral alteration information using WorldView-3 data, *Geoscience Frontiers*, 8, 5, 1051-1062. https://doi.org/10.1016/j.gsf.2016.10.008

Sykioti O., Ganas, A., Vasilatos Ch. and Kypritidou, Z., 2022. Detection of mineralized zones at an igneous intrusion in the Koutala islet, Lavreotiki, Greece using Sentinel-2 satellite data and mineralogical analysis. 16th International Congress of the Geological Society of Greece, 17-19 October 2022, Patras, Greece. Bulletin of the Geological Society of Greece, Sp. Publ. 10, pp. 388-389, ISBN: 978-960-98709-8-6.

Tompolidi, A., Sykioti, O., Koutroumbas, K., Parcharidis, I., 2020. Spectral Unmixing for Mapping a Hydrothermal Field in a Volcanic Environment Applied on ASTER, Landsat-8/OLI, and Sentinel-2 MSI Satellite Multispectral Data: The Nisyros (Greece) Case Study. Remote Sensing, 12, 4180. https://doi.org/10.3390/rs12244180

Van der Meer, F., Van der Werff, H., Van Ruitenbeek, F., Hecker, C., Bakker, H., Noomen, M., Van der Meidje, M., Carranza, E. J. M., de Smeth, B., & Woldai, T., 2012. Multi and hyperspectral geologic remote sensing: A review. *International Journal of Applied Earth Observation and Geoinformation*, 14(1), 112–128. https://doi.org/10.1016/j.jag.2011.08.002

Van der Meer, F., and Van der Werff, H.M.A., 2014. Potential of ESA's Sentinel-2 for geological applications. *Remote Sensing of Environment*, 148, 124–133. https://doi.org/10.1016/j.rse.2014.03.022

Van der Meer, F., Kopackova, V., Kaicka, L., Harald, M. A., Van der Werff, H., van Ruitenbeek, F. J. A., & Bakker, W. H., 2018. Wavelength feature mapping as a proxy to mineral chemistry for investigating geologic systems: An example from the Rodalquilar epithermal system. *International Journal of Applied Earth Observation and Geoinformation*, 64, 237–248. https://doi.org/10.1016/j.jag.2017.09.008

Van der Werff, H.M.A., Van der Meer, F.D., 2015. Sentinel-2 for mapping iron absorption feature parameters. *Remote Sensing*, 7, 12635–12653. https://doi.org/10.3390/rs71012635

Van der Werff, H., Van der Meer, F., 2016. Sentinel-2A MSI and Landsat 8 OLI provide data continuity for geological remote Sensing. *Remote Sensing*, 8, 883. https://doi.org/10.3390/rs8110883

Vasilatos, C., Economou-Eliopoulos, M., 2018. Fossilized Bacteria in Fe-Mn-Mineralization: Evidence from the Legrena Valley, W. Lavrion Mine (Greece). *Minerals*, 8, 107. https://doi.org/10.3390/min8030107

Vasilatos, C., Kampouroglou, E.E., Megremi, I., Economou-Eliopoulos, M., 2022. Bio-Geochemical Processes: Insights from Fe-Mn Mineralization in the Aegean Sea (Greece). *Minerals*, 12, 1303. https://doi.org/10.3390/min12101303

Vasuki, Y., Yu, L., Holden, E., Kovesi, P., Wedge, D., Grigg, A.H., 2019. The spatial-temporal patterns of land cover changes due to mining activities in the Darling Range, Western Australia: A Visual Analytics Approach. *Ore Geology Reviews*, 108, 23–32, https://doi.org/10.1016/j.oregeorev.2018.07.001

Voudouris, P., Mavrogonatos, C., Rieck, B.; Kolitsch, U., Spry, P.G., Scheffer, C., Tarantola, A., Vanderhaeghe, O., Galanos, E., Melfos, V., et al., 2018. The Gersdorffite-Bismuthinite-Native Gold Association and the Skarn-Porphyry Mineralization in the Kamariza Mining District, Lavrion, Greece. *Minerals*, 8, 531. https://doi.org/10.3390/min8110531

Voudouris, P., Melfos, V., Spry, P., Bonsall, T., Tarkian, M., Economou-Eliopoulos, M., 2008. Mineralogical and fluid inclusion constraints on the evolution of the Plaka intrusion-related ore system, Lavrion, Greece. *Mineralogy Petrology*, 93, 79-110. https://doi.org/10.1007/s00710-007-0218-0

Vural, A., Akpinar, I., Ferkan Sipahi, F., 2021. Mineralogical and chemical characteristics of clay areas, Gu¨mu¨ shane Region (NE Turkey), and their detection using the Crosta technique with Landsat 7 and 8 images. *Natural Resources Research*, 30, 6, 3955–3985. https://doi.org/10.1007/s11053-021-09912-7

Yamaguchi, Y., Kahle, A.B., Tsu, H., Kawakami, T., Pniel, M., 1998. Overview of Advanced Spaceborne Thermal Emission and Reflection Radiometer (ASTER). *IEEE Transactions on Geoscience and Remote Sensing*, 36, 1062–1071. https://doi.org/10.1109/36.700991

Yamaguchi, Y., Naito, C., 2003. Spectral indices for lithologic discrimination and mapping by using the ASTER SWIR bands. *International Journal of Remote Sensing*, 24, 4311–4323. https://doi.org/10.1080/01431160110070320

Yang, M., Ren, G., Han, L., Yi, H., Gao, T., 2018. Detection of Pb–Zn mineralization zones in west Kunlun using Landsat 8 and ASTER remote sensing data. *Journal of Applied Remote Sensing*, 12, 026018, https://doi.org/10.1117/1.JRS.12.026018

Yokoya, N., Chan, J.C.W., Segl, K., 2016. Potential of resolution-enhanced hyperspectral data for mineral mapping using simulated EnMAP and Sentinel-2 images. *Remote Sensing*, 8, 172, https://doi.org/10.3390/rs8030172